Photoproduction of two charged pions off protons in the resonance region

A. V. Sarantsev,[3] E. Klempt,[1,2,*] K. V. Nikonov,[2] P. Achenbach,[1] V. D. Burkert,[1] V. Crede,[4] V. Mokeev,[1] J. S. Alvarado,[25] M. J. Amaryan,[34] H. Atac,[40] L. Baashen,[17] N. A. Baltzell,[1,39] L. Barion,[20] M. Bashkanov,[45] M. Battaglieri,[21] B. Benkel,[22] F. Benmokhtar,[14] A. Bianconi,[42,24] A. S. Biselli,[15,8] F. Bossù,[10] S. Boiarinov,[1] K.-Th. Brinkmann,[35] W. J. Briscoe,[18] T. Cao,[1] R. Capobianco,[12] D. S. Carman,[1] J. C. Carvajal,[17] P. Chatagnon,[1] M. Contalbrigo,[20] A. D'Angelo,[22,37] N. Dashyan,[47] R. De Vita,[21,1] M. Defurne,[10] A. Deur,[1] S. Diehl,[35,12] C. Djalali,[33,39] R. Dupre,[25] H. Egiyan,[1] A. El Alaoui,[41] L. El Fassi,[29] L. Elouadrhiri,[1] P. Eugenio,[4] S. Fegan,[45] A. Filippi,[23] K. Gates,[44] G. Gavalian,[1,30] D. I. Glazier,[44] R. W. Gothe,[39] L. Guo,[17,1] K. Hafidi,[5] H. Hakobyan,[41] M. Hattawy,[34] D. Heddle,[11,1] A. Hobart,[25] M. Holtrop,[30] Y. Ilieva,[39,18] D. G. Ireland,[44] E. L. Isupov,[38] H. Jiang,[44] H. S. Jo,[27] K. Joo,[12] M. Khandaker,[32,†] W. Kim,[27] F. J. Klein,[9] V. Klimenko,[5] A. Kripko,[35] V. Kubarovsky,[1] L. Lanza,[22] P. Lenisa,[20,16] I. J. D. MacGregor,[44] D. Martiryan,[47] V. Mascagna,[42,24] D. Matamoros,[25] B. McKinnon,[44] T. Mineeva,[41] C. Munoz Camacho,[25] P. Nadel-Turonski,[1,‡] K. Neupane,[39] S. Niccolai,[25] G. Niculescu,[26] M. Osipenko,[21] A. I. Ostrovidov,[4] M. Ouillon,[29] P. Pandey,[28] M. Paolone,[31] L. L. Pappalardo,[20,16] S. J. Paul,[43] E. Pasyuk,[1] W. Phelps,[11,1] M. Pokhrel,[34] S. Polcher Rafael,[10] J. W. Price,[6] Y. Prok,[34,46] A. Radic,[41] T. Reed,[17] J. Richards,[12] M. Ripani,[21] G. Rosner,[44] A. A. Rusova,[38] C. Salgado,[32] S. Schadmand,[19] A. Schmidt,[18] R. A. Schumacher,[8] Y. G. Sharabian,[1] E. V. Shirokov,[38] S. Shrestha,[40] N. Sparveris,[40] M. Spreafico,[21] S. Strauch,[39,18] J. A. Tan,[27] R. Tyson,[1] M. Ungaro,[1] L. Venturelli,[42,24] T. Vittorini,[21] H. Voskanyan,[47] E. Voutier,[25] D. Watts,[45] X. Wei,[1] M. H. Wood,[7,39] L. Xu,[25] N. Zachariou,[45] Z. W. Zhao,[13] and M. Zurek[5]

(CLAS Collaboration)

[1]*Thomas Jefferson National Accelerator Facility, Newport News, Virginia 23606, USA*

[2]*Helmholtz-Institut für Strahlen- und Kernphysik, Universität Bonn, 53115 Bonn, Germany*

[3]*NRC Kurchatov Institute, PNPI, Gatchina 188300, Russia*

[4]*Florida State University, Tallahassee, Florida 32306, USA*

[5]*Argonne National Laboratory, Argonne, Illinois 60439, USA*

[6]*California State University, Dominguez Hills, Carson, California 90747, USA*

[7]*Canisius College, Buffalo, New York, USA*

[8]*Carnegie Mellon University, Pittsburgh, Pennsylvania 15213, USA*

[9]*Catholic University of America, Washington, DC 20064, USA*

[10]*IRFU, CEA, Université Paris-Saclay, F-91191 Gif-sur-Yvette, France*

[11]*Christopher Newport University, Newport News, Virginia 23606, USA*

[12]*University of Connecticut, Storrs, Connecticut 06269, USA*

[13]*Duke University, Durham, North Carolina 27708-0305, USA*

[14]*Duquesne University, 600 Forbes Avenue, Pittsburgh, Pennsylvania 15282, USA*

[15]*Fairfield University, Fairfield Connecticut 06824, USA*

[16]*Università di Ferrara, 44121 Ferrara, Italy*

[17]*Florida International University, Miami, Florida 33199, USA*

[18]*The George Washington University, Washington, DC 20052, USA*

[19]*GSI Helmholtzzentrum für Schwerionenforschung GmbH, D-64291 Darmstadt, Germany*

[20]*INFN, Sezione di Ferrara, 44100 Ferrara, Italy*

[21]*INFN, Sezione di Genova, 16146 Genova, Italy*

[22]*INFN, Sezione di Roma Tor Vergata, 00133 Rome, Italy*

[23]*INFN, Sezione di Torino, 10125 Torino, Italy*

[24]*INFN, Sezione di Pavia, 27100 Pavia, Italy*

[25]*Université Paris-Saclay, CNRS/IN2P3, IJCLab, 91405 Orsay, France*

[26]*James Madison University, Harrisonburg, Virginia 22807, USA*

[27]*Kyungpook National University, Daegu 41566, Republic of Korea*

[28]*Massachusetts Institute of Technology, Cambridge, Massachusetts 02139-4307, USA*

[29]*Mississippi State University, Mississippi State, Mississippi 39762-5167, USA*

[30]*University of New Hampshire, Durham, New Hampshire 03824-3568, USA*

[31]*New Mexico State University, PO Box 30001, Las Cruces, New Mexico 88003, USA*

[*]Contact author: klempt@hiskp.uni-bonn.de

[†]Present address: Idaho State University, Pocatello, Idaho 83209.

[‡]Present address: University of South Carolina, Columbia, South Carolina 29208.

[32]*Norfolk State University, Norfolk, Virginia 23504, USA*
[33]*Ohio University, Athens, Ohio 45701, USA*
[34]*Old Dominion University, Norfolk, Virginia 23529, USA*
[35]*II. Physikalisches Institut der Universität Gießen, 35392 Gießen, Germany*
[36]*Rensselaer Polytechnic Institute, Troy, New York 12180-3590, USA*
[37]*Università di Roma Tor Vergata, 00133 Rome, Italy*
[38]*Skobeltsyn Institute of Nuclear Physics, Lomonosov Moscow State University, 119234 Moscow, Russia*
[39]*University of South Carolina, Columbia, South Carolina 29208, USA*
[40]*Temple University, Philadelphia, Pennsylvania 19122, USA*
[41]*Universidad Técnica Federico Santa María, Casilla 110-V, Valparaíso, Chile*
[42]*Università degli Studi di Brescia, 25123 Brescia, Italy*
[43]*University of California Riverside, 900 University Avenue, Riverside, California 92521, USA*
[44]*University of Glasgow, Glasgow G12 8QQ, United Kingdom*
[45]*University of York, York YO10 5DD, United Kingdom*
[46]*University of Virginia, Charlottesville, Virginia 22901, USA*
[47]*Yerevan Physics Institute, 375036 Yerevan, Armenia*

(Received 27 November 2024; accepted 18 February 2025; published 31 March 2025)

Photoproduction of charged pions pairs off protons is studied within the invariant masses of the final state hadrons from 1.6 to 2.4 GeV at the Thomas Jefferson National Accelerator Facility with the CLAS detector. The total and differential cross sections and spin-density matrix elements are presented for the isobars $p\rho^0(770)$, $\Delta(1232)^{++}\pi^-$, and $\Delta(1232)^0\pi^+$. The data are included in the Bonn-Gatchina coupled-channel analysis and provide the information necessary to determine the branching fractions of $N\rho(770)$ decays for most known N^* and Δ^* resonances. For the first time, the $N\rho$ branching ratios are obtained here from an event-based likelihood to $\gamma p \to \pi^+\pi^- p$.

DOI: 10.1103/PhysRevC.111.035203

I. INTRODUCTION

Photoproduction of charged pion pairs off protons arises from rich dynamics. At high energies, neutral $\rho(770)$ mesons contribute significantly to the cross section: the incident photon can convert into a vector meson, e.g., a $\rho^0(770)$ meson, and the virtual vector meson may then scatter off the proton via Pomeron or Reggeon exchange [1]. Understanding these processes in terms of quark and gluon interactions remains a major challenge for quantum chromodynamics (see Ref. [2] for a review).

At lower energies, additional production modes become important [3]: The initial photon can dissociate the proton into a $\Delta(1232)^{++}$ and a π^- meson through a contact interaction (Kroll-Ruderman mechanism). The $\Delta(1232)$ and higher-mass N and Δ excitations can be produced as intermediate isobars, decaying into the $N\pi\pi$ final state in a cascade process. The two final-state pions may interact, forming scalar, vector, or tensor mesons.

In this paper, we report a detailed study of the reaction

$$\gamma p \to \pi^+\pi^- p. \tag{1}$$

Mass and angular distributions for γp invariant masses up to 2.15 GeV have been presented in a Letter [4], where the total cross section and photocouplings of four-star N and Δ resonances below 2 GeV were determined. These distributions, along with data on reaction (1) with linearly polarized photons and transversely polarized protons [5], are included in a large database used for a coupled-channel analysis. Here, part of the data on reaction (1) are used event-by-event in an event-based likelihood fit. Results on the properties of N^* and Δ^* resonances will be presented elsewhere [6].

The two-pion production process has been studied before in pion-, photo-, and electroproduction (for electroproduction, see Refs. [7] and [8], and references therein).

Pion-induced experiments. Early analyses of πN scattering into three-body final states utilized bubble chambers. The low-energy region covering the $N(1440)1/2^+$ resonance was studied in Refs. [9,10]. The resonance region was investigated in different charge combinations of the $N\pi\pi$ final state, covering the 1390–1535 MeV [11,12], 1400–2000 MeV [13], 1500–1740 MeV [14], and 1400–1700 MeV [15] mass ranges.

The first counter experiments focused on the threshold region to study the breaking of chiral symmetry [16–24]. The energy range was later expanded when the Crystal Ball detector was moved to BNL, where the reaction $\pi^- p \to \pi^0\pi^0 n$ was studied up to $\sqrt{s} = 1520$ MeV [25]. Recently, the HADES Collaboration reported results on the reaction $\pi^- p \to \pi^+\pi^- p$ at four beam momenta ranging from 650 to 786 MeV, deriving excitation functions of various partial waves and of the $\Delta(1232)\pi$, $Nf_0(500)$, and $N\rho(770)$ isobar configurations [26].

Photoproduction experiments with bubble chambers. The first photoproduction experiments were carried out at photon energies in the $3 < E_\gamma < 8$ GeV range exploiting bubble chambers with correspondingly low statistics [27–31].

Photoproduction experiments at MAMI. Photoproduction using a counter experiment was first studied at the electron accelerator MAMI for energies up to 0.8 GeV [32];

three different two-pion states ($p\pi^+\pi^-$, $p\pi^0\pi^0$, $n\pi^+\pi^0$) were studied and cascade decays via $\Delta^0(1232)\pi^0$ were observed [33]. The decays were tentatively assigned to $N(1440)1/2^+$ or $N(1520)3/2^- \to \Delta^0(1232)\pi^0$ decays [34]. The helicity dependence of the $\gamma p \to p\,2\pi^0$ [35,36] and $\gamma p \to \pi^+\pi^- p$ [36,37] cross sections indicated a preference for the decay sequence $N(1520)3/2^- \to \Delta^0(1232)\pi^0$. The beam helicity asymmetry was compared to models, in the case of $\pi^0\pi^0$ production with reasonable agreement, in the case of $\pi^+\pi^0$ production with large discrepancies [36,37] for all models used. In Refs. [35,36,38], the $\pi^0\pi^0$ production threshold was investigated and predictions of the chiral perturbation theory for the threshold behavior were confirmed.

In Ref. [39], the differential cross sections for $2\pi^0$ photoproduction were expanded into spherical harmonics and moments. Large contributions from spin-parity $J^P = 3/2^-$ waves were required below the $N(1520)3/2^-$ resonance. This effect was tentatively ascribed to contributions of the wide $\Delta(1700)3/2^-$ or to rescattering effects. The A2 Collaboration compared $\pi^0\pi^0$ photoproduction off free protons with photoproduction off quasifree protons and neutrons bound in deuterons [40]. The results on bound and free protons agree in shape reasonably well, although the cross section for the quasifree protons was found to be smaller than the cross section measured with an H_2 target. The cross section for the reaction $\gamma n \to \pi^0\pi^0 n$ showed a much less pronounced valley between the peaks due to the second and third resonance regions at about 1.5 and 1.7 GeV. The peak at about 1.7 GeV from the γp initial state was mainly assigned to the $N f_0(500)$ decay mode, while for γn this structure was assigned to the $\Delta(1232)^0\pi^0$ decay mode. Apparently, different resonances in the third resonance region are predominantly produced off protons or off neutrons.

The A2 Collaboration determined the double-polarization observable E, and helicity-dependent cross sections $\sigma_{1/2}$ and $\sigma_{3/2}$ were reported for photoproduction of π^0 pairs off quasifree protons and neutrons, and determined the helicity- and isospin-dependent structure of the $\gamma N \to N\pi^0\pi^0$ reaction [41]. The polarization observables P_x, P_y (unpolarized beam, target polarized in the x, y directions), $P_x^\odot, P_y^\odot$ (circularly polarized beam, target polarized in the x, y directions) were measured [42]. A partial wave analysis was performed that included Born terms and a sum of s-channel Breit-Wigner resonances.

Photoproduction experiments at LEPS. The Graal Collaboration studied the energy range up to $E_\gamma = 1.5$ GeV; the total cross section showed strong peaks at $W = 1.5$ and 1.7 GeV for $\gamma p \to p\,2\pi^0$ [43] and for $\gamma n \to n\,2\pi^0$ [44]. The LEPS Collaboration studied the differential cross section and photon-beam asymmetry for the reaction $\gamma p \to \pi^-\Delta(1232)^{++}$ at forward π^- angles [45].

Photoproduction experiments at ELSA. The reaction (1) was studied by the SAPHIR Collaboration [46] throughout the resonance region. The total cross section up to $E_\gamma = 2.6$ GeV was determined as well as the $\rho^0(770)$, $\Delta(1232)^{++}$, and $\Delta(1232)^0$ excitation functions and the t dependence of the production of the isobars.

The results of the CBELSA/TAPS Collaboration on $\gamma p \to p\,2\pi^0$ were included in a coupled-channel analysis of a larger data set and provided masses, widths, helicity amplitudes, and decay frequencies for resonances up to 1700 MeV [47,48]. Later, the photon energy range was extended and photon polarization data were included. The coupled-channel analysis yielded a large number of cascade decays [49–51]. It was shown that baryon resonances with a component in the wave function in which both oscillators are simultaneously excited have a significant fraction of decays into orbitally or radially excited mesons or baryons; resonances with only one oscillator deexcite mostly into mesons and baryons without orbital or radial excitations. The findings were confirmed in a recent analysis of the reaction $\vec{\gamma}\vec{p} \to p\,2\pi^0$ with linearly polarized photons and transversely polarized protons [52].

Photoproduction experiments at Jefferson Lab. Photoproduction of $\rho(770)$ mesons off protons has been studied by the CLAS Collaboration for E_γ between 3.19 and 3.91 GeV and squared momentum transfers $-t$ from 0.1 to 5 GeV^2 [53]. The beam helicity asymmetry was studied in the energy range $1.35 < E_\gamma < 2.3$ GeV, but without firm conclusions on the contributing resonances [54]. In the energy range from 3.0 to 3.8 GeV, moments in the $\pi\pi$ angular distributions were extracted in Ref. [55]. As discussed above, contributions from the excitation spectrum of the nucleon were identified in [4]. A comparison of the properties of the resonances produced in photo- and electroproduction showed inconsistent results for the $N(1720)3/2^+$ decays to $\Delta\pi$ and $N\rho(770)$, which were only resolved by introducing an additional resonance $N'(1720)3/2^+$ [56]. Recently, the spin-density matrix elements were measured for photon energies in the 8.2 to 8.8 GeV range by the GlueX Collaboration for $\rho(770)$ photoproduction with natural and unnatural parity exchange [57] and for the $\Delta(1232)^{++}\pi^-$ final state [58].

In this paper, we present details of the extraction of the $\gamma p \to p\pi^+\pi^-$ reaction reported in a Letter [4]. We give a short description of the CLAS detector and discuss the four event topologies: events with three particles detected or with p, π^+, or π^- missing. A randomly selected subsample of the data are included in the BnGa coupled-channel analysis in an event-by-event likelihood fit. The analysis yields Dalitz plots, mass and angular distributions, the total cross section and excitation functions for $\gamma p \to \Delta(1232)^{++}\pi^-$, $\Delta(1232)^0\pi^+$, $p\rho^0(770)$, and $p f_2(1270)$, differential cross section as a function of squared momentum transfer t, spin-density matrix elements for $p\rho^0(770)$, and branching ratios of N^* and Δ^* resonances for their decays into $N\rho(770)$. Analysis details and branching ratios for N^* and Δ^* decays into $\Delta(1232)\pi$ and $N^*\pi$ will be presented elsewhere [6]. The new results profit from the large number of events from reaction (1) and the extended energy range.

II. THE CLAS EXPERIMENT AND EVENT SELECTION

The results presented here were derived using the CEBAF Large Acceptance Spectrometer (CLAS) [59] in Hall B at the Thomas Jefferson National Accelerator Facility during the "g11a" data taking period in 2004. The photon beam was produced by an unpolarized electron beam of 4.019 GeV energy. The beam current ranged from 60 to 75 nA. The electron beam was impinged on a gold foil radiator with a thickness

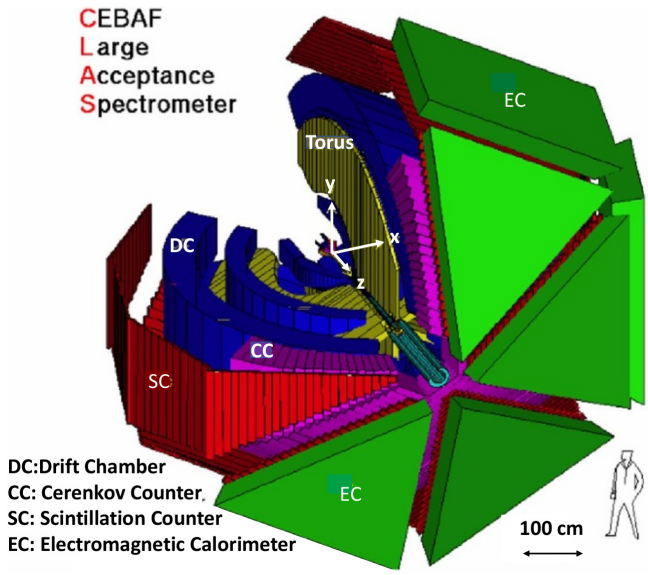

FIG. 1. Cutaway view of the CLAS detector [59] illustrating the torus magnet, three regions of drift chambers (R1–R3), Cherenkov counters (CC), time-of-flight (TOF) scintillators, and electromagnetic calorimeters (EC). The CLAS detector was approximately 10 m in diameter.

of 10^{-4} radiation lengths. The beam delivered tagged photons with energies from 1.6 to 2.6 GeV. The photon energies were determined by detecting scattered electrons in the tagging spectrometer [60,61].

A. Target and photon beam

The tagged photon flux on the target within the data acquisition live time was obtained by the standard CLAS *gflux* method [62]. The number of photons for each tagger counter was calculated independently as $N_\gamma = \epsilon N_{e^-}$, where N_{e^-} is the number of electrons detected by a tagger counter and ϵ is the tagging ratio. The tagging ratio was determined by placing a total absorption counter directly in the photon beam at low intensity and determining the ratio of the number of beam photons and the number of electrons detected in coincidence in the tagger. The global normalization uncertainty derived from the run-to-run variance and the estimated normalization variance with the electron beam current together were found to be 1%, employing the method described in Ref. [63].

The photons hit a 40-cm-long liquid H_2 target. Temperature and pressure of this cryogenic target were monitored throughout the run period. The mean calculated density of H_2, $0.0718\,\mathrm{g/cm^3}$, was nearly constant with relative fluctuations of about 0.1% [63,64].

B. The CLAS detector

The CLAS detector, shown in Fig. 1, was designed around six superconducting coils arranged in a hexagonal configuration that produced an approximately toroidal magnetic field surrounding the beamline. The magnetic field bent charged particles through the regions of multilayer drift chambers for momentum measurements. Drift chambers were positioned between the superconducting coils within six sectors in azimuthal ϕ, each spanning approximately 60°. Charged particles reconstructed in the fiducial volume and produced at a momentum of 1 GeV were measured with average angular resolutions of $\sigma(\Theta), \sigma(\phi) \sim 2$ mrad and with a momentum resolution of $\sigma(p)/p \leqslant 0.5\%$ [65].

The start counter scintillators [66] (not shown) with a time resolution of 260 ps surrounded the target cell and were used to determine the start time of the event. A set of 342 time-of-flight (TOF) scintillators was used for particle identification [67]. Their timing resolution ranged between 150 and 250 ps, depending on the length of the paddle. The Cherenkov counters and electromagnetic calorimeters were used for the detection of electrons and neutral particles [68]. A coincidence between the start counter and TOF scintillators in at least two of the six CLAS sectors was required to trigger the data acquisition. Some TOF paddles were dead or showed an excessive rate. Hits in 22 paddles were later removed from further analysis. During the g11a run period, the integrated luminosity was $70\,\mathrm{pb}^{-1}$, and $\sim 2 \times 10^{10}$ triggers were recorded.

C. Event selection

The selection of $\pi^+\pi^- p$ photoproduction events was carried out within the framework developed by the CLAS Collaboration [4,69] and which was applied already to the full data sample used in Ref. [69]. Here we will highlight the specific features of this approach, which are relevant for physics analysis on an event-by-event basis.

Fiducial cuts. The CLAS detector contained insensitive regions for particle detection. These insensitive regions were located in the regions blocked by the torus coils, as well as at very forward and very backward angles in the laboratory frame [59]. The final-state particles were selected [69] to be within the "fiducial" regions with reliable particle detection efficiency, away from the insensitive regions. In addition, kinematic regions were excluded where the particle detection acceptance was less than 5%.

In a first step, fiducial cuts based on the polar (Θ) and azimuthal (ϕ) angles of a particle were applied. Tracks with a polar angle $\Theta < 27°$ in the forward direction were removed. A fiducial cut on the azimuthal (ϕ) angle removed tracks close to insensitive regions in the six sectors, with the cut on Θ being ϕ dependent. Figure 2 shows the distribution of Θ versus ϕ for charged pions and protons for the first sector. The event distributions for the other sectors look very similar. These fiducial cuts were defined iteratively, with preliminary and final particle identification.

Timing information was used to clean the event sample. A cut of 1.5 ns was applied for the time difference between tagger time and the start time derived from the CLAS start counters. The kinematic fit probed all photons within this time window.

Monte Carlo. The CLAS detector is simulated with the standard CLAS gsim package [70] and an event generator based on the JM05 version of the $\pi^+\pi^- p$ reaction model [71,72]. The Monte Carlo events undergo the same reconstruction and selection chain as for data events.

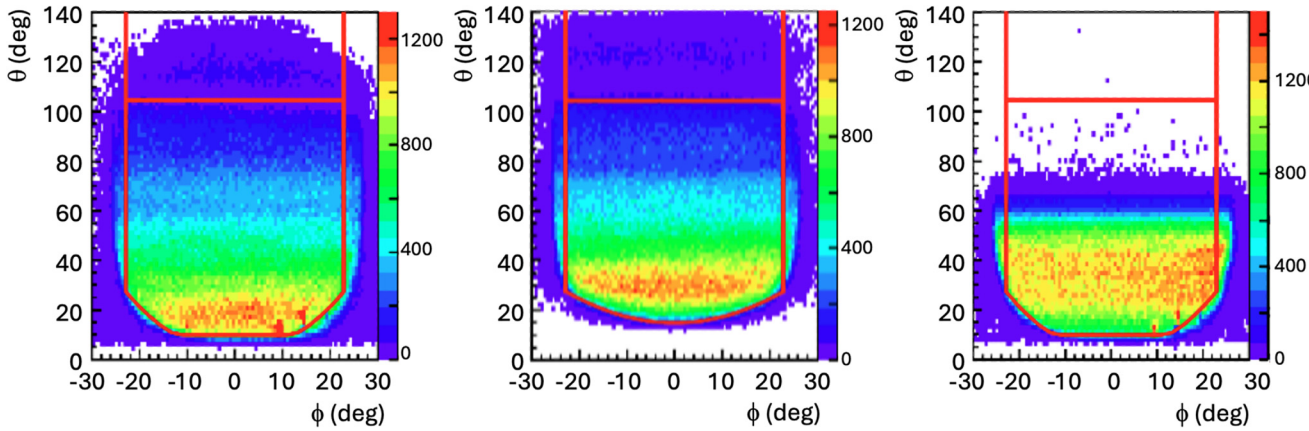

FIG. 2. Polar (Θ) versus azimuthal (ϕ) angular distributions for identified π^+ (left), π^- (middle), and protons (right) in one of the six sectors of the CLAS spectrometer. Fiducial cuts are shown in red.

Kinematic fit. The sample of events with two or three tracks consisted of four mutually exclusive topologies: one with all three final-state hadrons detected and three others in which one out of the three final-state hadrons was missing. In events with all three particles detected, the energy given by the tagger (E_t) was compared with the energy calculated from the reconstructed final-state particles (E_p). The momenta of the charged particles were corrected for the energy loss in materials of the target assembly [73]. The tagged-photon energies were also corrected taking into account all known tagger focal-plane mechanical deformations. After corrections, the E_t/E_p distribution was centered at 1 with a width of 0.52%, which quantifies the relative energy uncertainty $\Delta E/E$ related to the reconstructed photon energy and the invariant mass of the event. A kinematic fit with four constraints (energy and momentum conservation) adjusts the total energy within this range.

A kinematic fit was used to select events due to the $\gamma p \to \pi^+\pi^- p$ reaction [74]. Events with the three particles detected were constrained by energy and momentum conservation (4C fit); for events with a missing π^-, π^+ or p, its momentum had to be determined in the kinematic fit, leaving one constraint (1C fit). We refer to these topologies as C_0 (4C) and C_i, $i = 1, 2, 3$ (1C).

In kinematic fits, the observables p, λ, and ϕ (p = modulus of the particle momentum, $\lambda = \cos\Theta$, ϕ = azimuthal angle) are combined into a vector y. The measured quantities η deviate from y by ϵ,

$$\eta = y + \epsilon. \tag{2}$$

The improved values of y are determined by the kinematic fit. The fit determines the value of the *confidence level* (CL), defined as

$$\mathrm{CL} = \int_{\chi^2}^{\infty} f(x;n)dx, \tag{3}$$

where $f(x;n)$ is the probability density function of the χ^2 distribution with n degrees of freedom. Under ideal conditions, a flat CL distribution is expected. Given the increase in the distribution towards zero, small values of CL may indicate a significant fraction of background events. Here, events with CL < 0.1 are rejected; 72% of the events have CL $> 10\%$. Figure 3 shows the confidence level distribution for events passing the 4C fit. The distribution for measured events shows a reasonably flat distribution and a rise at low CL. This might signal strong background contributions. These contributions are discussed in the next subsection.

The quality of the error definition can be estimated from the pull distributions. The pull is defined as

$$\frac{\epsilon_i}{\sigma(\epsilon_i)} = \frac{\eta_i - y_i}{\sigma(\eta_i) - \sigma(y_i)}, \tag{4}$$

where $\sigma(y_i)$ is the standard deviation of y_i found in the kinematic fit. When the errors of the measured quantities are correctly determined, the pulls are normally distributed around zero with a standard deviation equal to unity. As an example, in Fig. 4 we show the pull distributions for events with the three measured particles (4C fit). All pull distributions can be described by Gaussian distributions centered at 0.00 ± 0.05 with $\sigma = 1.0 \pm 0.1$.

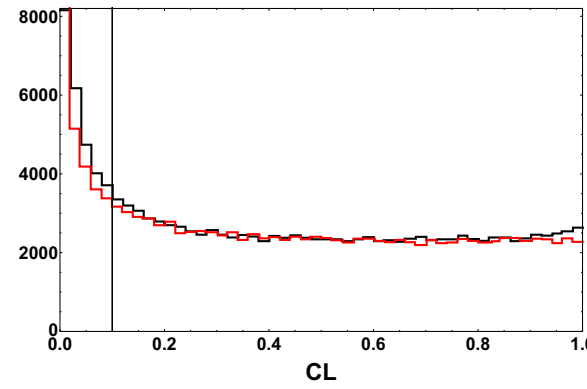

FIG. 3. Confidence level distributions for data (black) and Monte Carlo events (red). The number of Monte Carlo events is normalized to the number of data events.

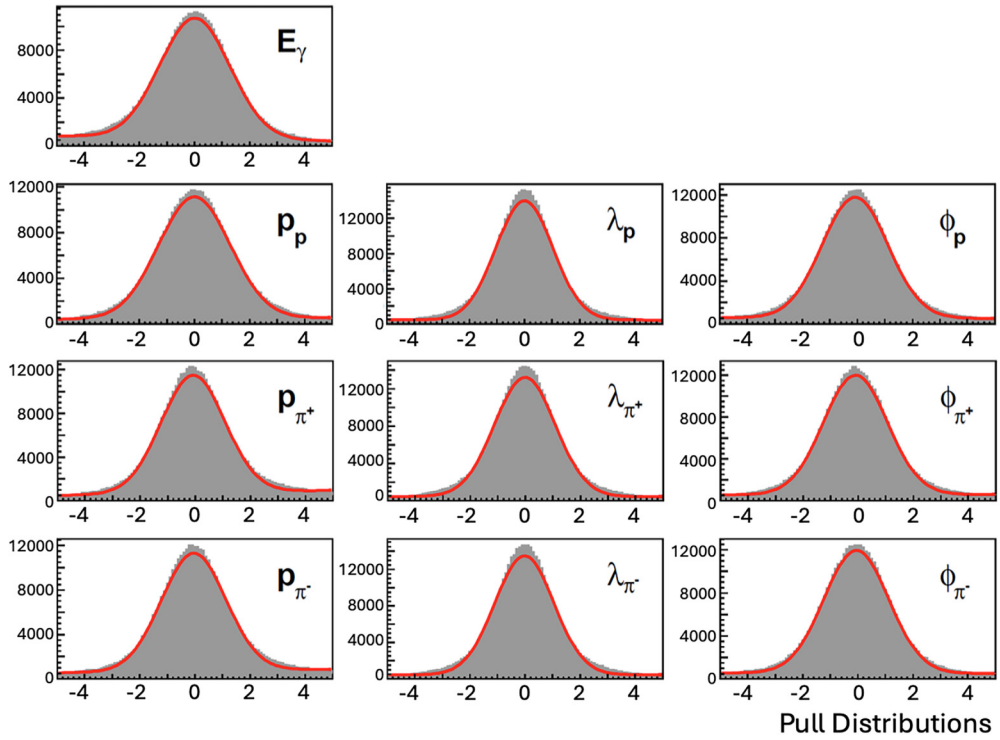

FIG. 4. Pull distributions for 4C events: number of events as a function of the pull [see Eq. (4)]. The pull distributions for 1C events are nearly identical.

D. The background

The selection of two-pion events due to reaction (1) relies upon kinematic fitting. The confidence level distribution indicates the presence of large background contributions. A contamination may come from three-pion events $\gamma p \to p\pi^+\pi^-\pi^0$ which could be reconstructed as a two-pion event or from badly measured two-pion events.

Both two- and three-pion events were simulated with their known cross sections. A realistic event generator based on the results reported in Refs. [71,72] was used for two-pion events. Three-pion events were generated using a phase space approximation.

Figure 5 shows events due to the two reactions with reconstructed p and π^+, with the missing mass computed under the assumption that they belong to reaction (1). The mean three-pion background for these events with a missing π^-, averaged over all kinematic bins, is 3.2%. Similar distributions show that the background for events with a missing p or π^+ is 2.5% or 1.3%. This fraction rises about linearly from zero at $E_\gamma = 0.9\,\text{GeV}$ to $(6 \pm 2)\%$ at $E_\gamma = 1.7\,\text{GeV}$. The three-pion background vanishes for events in which all three particles were reconstructed. Obviously, the three-pion background cannot be responsible for the large contribution with CL $< 10\%$.

Indeed, the mass and angular distributions of the events with CL $< 10\%$ are very similar to those with CL $> 10\%$. We conclude that events with CL $< 10\%$ are mostly true $p\pi^+\pi^-$ events that are not so well measured, or events with wrong particle identification. True two-pion events that form a spike at small values of CL have distributions over all kinematic variables similar to those of the events that pass the CL cut. A cut of CL < 0.1 reduces the acceptance by a factor of 0.72. Simulated $p\pi^+\pi^-$ events passed the CL cut at 10% with a probability of 75%. Of course, all simulated events are true $p\pi^+\pi^-$ events. The difference between the 75% acceptance for data and 72% for Monte Carlo events is compatible with the detailed studies in Ref. [74] that give a 3% systematic uncertainty on yield extractions due to mismatches of the kinematic fit between the data and Monte Carlo events. Hence

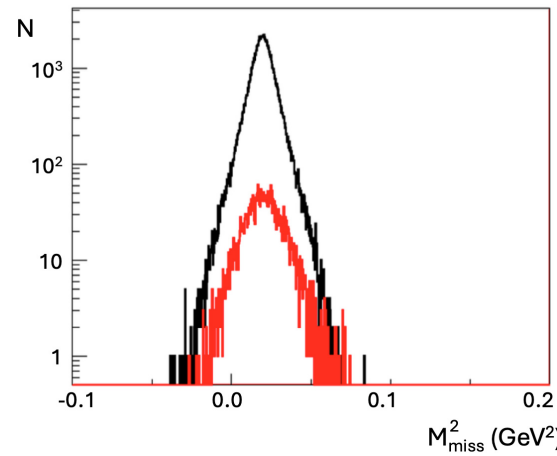

FIG. 5. Missing mass distribution for Monte Carlo events from $\gamma p \to p\pi^+\pi^-$ reactions with a missing π^- (black) and $\gamma p \to p\pi^+\pi^-\pi^0$ (red), reconstructed as two-pion events.

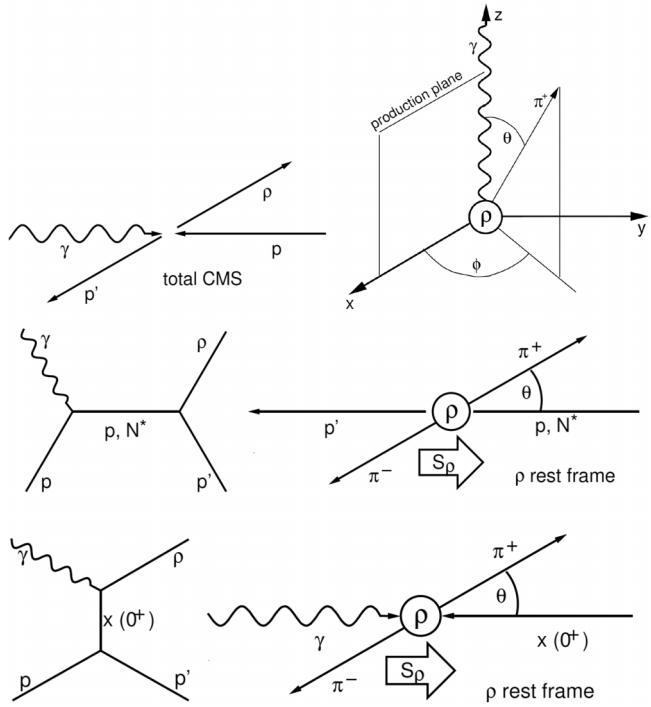

FIG. 6. In the center-of-mass system, the photon and proton collide having momenta of the same magnitude. One particle, here the π^+, and a properly chosen z axis are used to define the production plane and the angles Θ and ϕ in the $\rho^0(770)$ rest frame (top). For the helicity frame the photon direction (center) and in the Gottfried-Jackson frame the $\rho^0(770)$ direction (bottom) is chosen as the z axis. The helicity and Gottfried–Jackson frames are used to characterize s- and t-channel exchanges. S_ρ denotes the ρ spin, $X(0^+)$ stands for Pomeron exchange. (Adapted from [46].)

a correction factor of $1/(0.72 \pm 0.03)$ was applied to the obtained cross sections.

III. ANALYSIS

A. The coordinate frames

The three four-momenta of events in reaction (1) are defined by 12 variables. Energy-momentum conservation (four constraints) and requirement for the final state hadrons to be on shell (three constraints) reduce this number to five variables, which we choose as invariant masses $M_{\pi^+\pi^-}$, $M_{p\pi^+}$, $M_{p\pi^-}$ and two angles Θ and ϕ. The angles can be defined in different frames (see Fig. 6).

In the center-of-mass system (c.m.s.), the total momentum vanishes; it is related to the laboratory frame by a Lorentz boost along the z axis. Two further frames require a second Lorentz boost in the rest frame of one of the three two-particle systems, e.g., in the $\rho^0(770)$ rest frame; see Fig. 6. The z axis can then be chosen as the direction of the photon (Gottfried-Jackson frame) or in the direction of one of the three two-particle systems (helicity frame). The polar angle Θ is then defined as the angle between the decay momentum in the two-particle subsystem and the z axis. Figure 6 shows these angles in the $\rho^0(770)$ meson rest frame. For resonance production, the s-channel helicity conservation can be tested in the helicity frame. For particle (or Reggeized particle) exchange in the t channel, the photon spin can be transferred to the $\rho^0(770)$ meson, and the t channel helicity may be conserved.

TABLE I. The Bonn-Gatchina database used in the coupled-channel analysis in addition to the new data on $\gamma p \to p\pi^+\pi^-$. $\pi N \to \pi N$ stands for the real and imaginary parts of the partial-wave amplitudes for πN elastic and charge-exchange scattering derived by the GWU [75] or Karlsruhe-Helsinki [76] groups.

γp	$\to$	$\pi^0\pi^0 p$	$\pi^0\eta p$	$\pi^+\pi^- p$	ωp	$\pi N \to \pi N$	
γp	$\to$	πN	ηp	$\eta' p$	$K^+\Lambda$	$K^+\Sigma^0$	$K^0\Sigma^+$
γn	$\to$	πN	ηn	$K^0\Lambda$	$K^+\Sigma^-$		
$\pi^- p$	$\to$		ηn	$K^0\Lambda$	$K^0\Sigma^0$	$K^+\Sigma^-$	
$\pi^- p$	$\to$	$\pi^+\pi^- n$	$\pi^0\pi^0 n$	$\pi^0\pi^- p$	$\pi^+ p \to K^+\Sigma^+$		

B. The coupled-channel analysis

The BnGa database. The BnGa database covers all of the main results on pion- and photoinduced reactions. In particular, we used differential cross sections and polarization observables on the reactions shown in Table I. The *full data set* and the *event-based data sample*, as well as new CLAS data on $\vec{\gamma}\vec{p} \to p\pi^+\pi^-$ [5], are included in the BnGa database.

Also included are the real and imaginary parts of the elastic $\pi N \to \pi N$ scattering amplitudes from the GWU [75] or Karlsruhe-Helsinki [76] analysis. The full list of the data used can be found on the BnGa website [77]. Events with three particles in the final state are included in the fit event-by-event maximizing the log-likelihood. The difference of the χ^2 values from fits to distributions like differential cross sections, polarization asymmetries and the likelihood for three-particle final states is minimized in the fit. All data sets are given a weight to guarantee that they have an impact on the fit result but that they do not lead to a significantly worse fit to other data sets. In first studies, the weight of a new data set is increased until the overall χ^2 starts to increase.

The BnGa PWA approach. In the BnGa approach, the energy-dependent part of the photoproduction amplitude is described by a D matrix that is based on dispersion relations and a one-step subtraction. The amplitude is covariant and preserves analyticity and two-particle unitarity. The photoproduction amplitude contains coupling constants describing transitions from initial to final states via resonances and via nonresonant transitions. Resonances correspond to K-matrix poles. Further contributions with at most left-hand singularities are approximated by non-resonant terms. The angular momentum barrier is taken into account by Blatt-Weisskopf form factors. Rescattering within the three-body final state is taken into account. The explicit formulas are given elsewhere [6].

C. Full data set and event-based data sample

Overall, about 400 million $\pi^+\pi^- p$ events were selected. These events were used to derive the invariant mass and

angular distributions. The CLAS detector does not provide full angular coverage. To reconstruct a $p\pi^+\pi^-$ event, only two particles need to be detected, but some events may be lost. A dynamical model is therefore required.

For the *full data set*, the JM17 model developed by the JLab-MSU Collaboration [78,79] was used. This model has been successfully applied to describe the cross section for photo- and electroproduction (in the Q^2 range from 0.25 to 1.5 GeV^2) of two charged pions off protons. All ingredients of the model are identical when describing reactions induced by real or virtual photons. Hence, it was used for a model extrapolation of the cross sections published in Ref. [4]. This data set is referred to as the *full data set*.

The number of events is too large to use in event-based likelihood fits. Therefore, a subsample was employed, consisting of 75 512 4C fit events (C_0), 660 019 events with the π^- missing (C_1), 616 221 events with the π^+ missing (C_2), and 490 576 events with the proton missing (C_3). Although this subsample represents only a small fraction of the full data set, it allows event-based likelihood fits where all correlations within the three-particle dynamics are considered. As we shall see, the systematic uncertainties in the physics results significantly exceed the statistical uncertainties. Thus, the reduced statistics do not pose a problem.

The acceptance of the *event-based data sample* was determined by comparing reconstructed and generated Monte Carlo events weighted with the result of the BnGa coupled-channel analysis.

The resonance parameters were optimized by minimizing the negative logarithm of the likelihood function:

$$-\ln L = -\sum_{i=1}^{N_{\mathrm{data}}} \left(\ln \sigma_i - \ln \frac{1}{N_{\mathrm{MC}}} \sum_{j=1}^{N_{\mathrm{MC}}} \sigma_j \right), \tag{5}$$

where $\ln \sigma_i$ represents the natural logarithm of the differential cross section calculated for the reconstructed data events, normalized to the sum of the differential cross sections for the reconstructed Monte Carlo events.

There is an important difference between the use of the *full data set* and the *event-based data sample*. The full data set is used after integration of the fourfold differential cross sections over the three different sets of three variables. Thus nine mass and angular distributions are obtained and the fit model is used to describe these distributions. The important correlations between the variables is lost. In event-by-event likelihood fits, the full information encoded in the three four-vectors is taken into account; the correlation between the different variables is fully exploited.

The four topologies. The four topologies—fully reconstructed events and events with a missing proton, π^+, or π^-—represent single dynamical processes. Consequently, the mass and angular distributions across all four topologies should be described by a single fit. However, differences in acceptance among the topologies can lead to variations in observed shapes. A precise understanding of the detector's response is therefore mandatory.

The detector efficiency was calculated using a detailed geant simulation of the CLAS detector, known as gsim [70], and an event generator based on the older JM05 reaction model [71,72]. Using an event generator that simulates the reaction avoids the need to generate large Monte Carlo data sets in kinematic regions with low cross sections. However, the specific details of the reaction model are irrelevant to the likelihood fit.

Figure 7 presents acceptance-corrected angular distributions 0.04 wide bins in Θ of p, π^+, and π^- for the four topologies at $W = 2\,\mathrm{GeV}$ in a 25 MeV bin for the *full data set*. The consistency is very good. We conclude that the acceptance is reasonably well accounted for by the Monte Carlo simulation.

In Fig. 8, we present invariant mass distributions for the *event-based data sample* and the four topologies at $W = 2\,\mathrm{GeV}$. The experimental distributions are shown by crosses, the histogram represents the final fit. The distributions are not corrected for efficiency. We may expect very different distributions due to different acceptances for the four topologies. This is not the case. This proves that the solid angle coverage of the CLAS detector for detecting two out of three particles is surprisingly homogeneous.

In all four topologies, the $\pi^+\pi^-$ mass distributions show the important role of $\rho^0(770)$ meson production in photoproduction of two charged pions. The $p\pi^+$ mass distribution exhibits a strong peak due to $\Delta(1232)^{++}$ production. The masses and widths of the $\Delta(1232)^{++}$ seem to be reasonably consistent. Small differences can be noticed in the $p\pi^+$ invariant mass distribution in the higher-mass region and in the $p\pi^-$ invariant mass distribution in the lower-mass region. The threshold enhancement in the $p\pi^-$ mass distribution can be traced to the production of $\Delta(1232)^0$. It is much weaker than the production of $\Delta(1232)^{++}$. The large enhancement in the $p\pi^-$ invariant mass distribution centered at $\sim$1.8 GeV is a reflection of $\Delta(1232)^{++}$ and $p\rho^0(770)$ production.

A more detailed view is obtained by studying the angular distributions. These are shown in Fig. 9, again in four rows for the four topologies C_i. Similar conclusions can be drawn as for the mass distributions: the main features are well reproduced in the fit, while some small but significant inconsistencies are seen. A remarkable effect is seen for the b_i distributions: b_0, b_2, b_3 show a pronounced dip at $\cos\Theta_{\pi^-} \lessapprox 0$ which is not seen in b_1. In b_1 small discrepancies can be observed, but the dip is absent in both the experimental distribution and the fit.

Adding all four topologies will minimize the effects of small deviations of the Monte Carlo simulation and the response of the CLAS detector. In any case, we have made fits to the individual topologies $i = 0, 1, 2, 3$. The spread of the results obtained from these fits is included as part of the systematic uncertainty.

IV. RESULTS

A. Dalitz plots

Figure 10 shows the acceptance-corrected Dalitz plots from the *event-based data sample* for the reaction (1) in bins of 100 MeV in W from 1600 to 2150 MeV. In the figures, $M^2_{p\pi^-}$ is plotted versus $M^2_{p\pi^+}$, then $M^2_{p\pi^+}$ versus $M^2_{\pi^+\pi^-}$. For the Dalitz plots, the four topologies C_i are added.

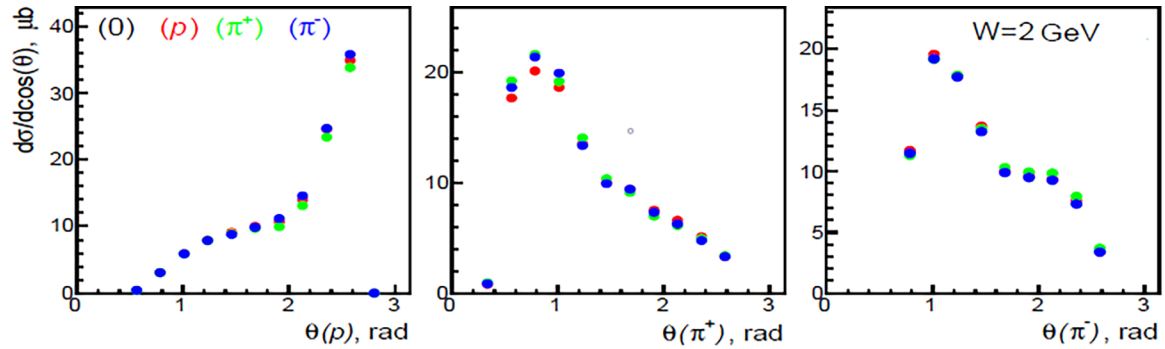

FIG. 7. Comparison of the differential cross sections $d\sigma/d\Theta$ at $W = 2\,\text{GeV}$ in a 25 MeV bin for the *full data set* for different missing particle topologies, where Θ is the polar angle of the proton or pion. The colors of the data points indicate the topology. The black points are not seen as they are covered by the other points.

Production of neutral $\rho(770)$ mesons is one of the most significant features of the reaction: it dominates the reaction above energies of $W > 1.80\,\text{GeV}$. Also very important, in particular at low energies, is the production of $\pi^-\Delta(1232)^{++}$. It is much larger than the production of $\pi^+\Delta(1232)^0$. The Clebsch-Gordan coefficients imply that high-mass N^* resonances decaying to $\pi\Delta(1232)$ contribute to $\pi^-\Delta(1232)^{++}$ nine times more than to $\pi^+\Delta(1232)^0$, for Δ^* resonances, the ratio is 9:4. The even higher yield of $\pi^-\Delta(1232)^{++}$ points to a production mode different from only resonance

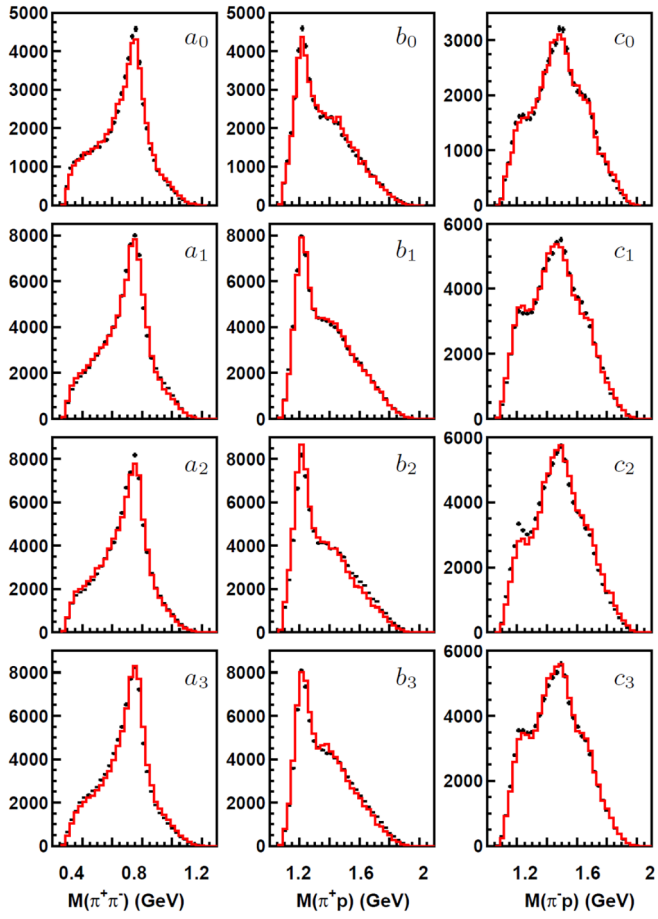

FIG. 8. The $\pi^+\pi^-$ (a), $p\pi^+$ (b), and $p\pi^-$ (c) mass distributions of events in the full data sample for the mass range $1.9 < W < 2.1\,\text{GeV}$ for the four topologies C_i, $i = 0, 1, 2, 3$. The distributions are not corrected for efficiency. The data are represented by crosses, our fit (in red) by the histogram.

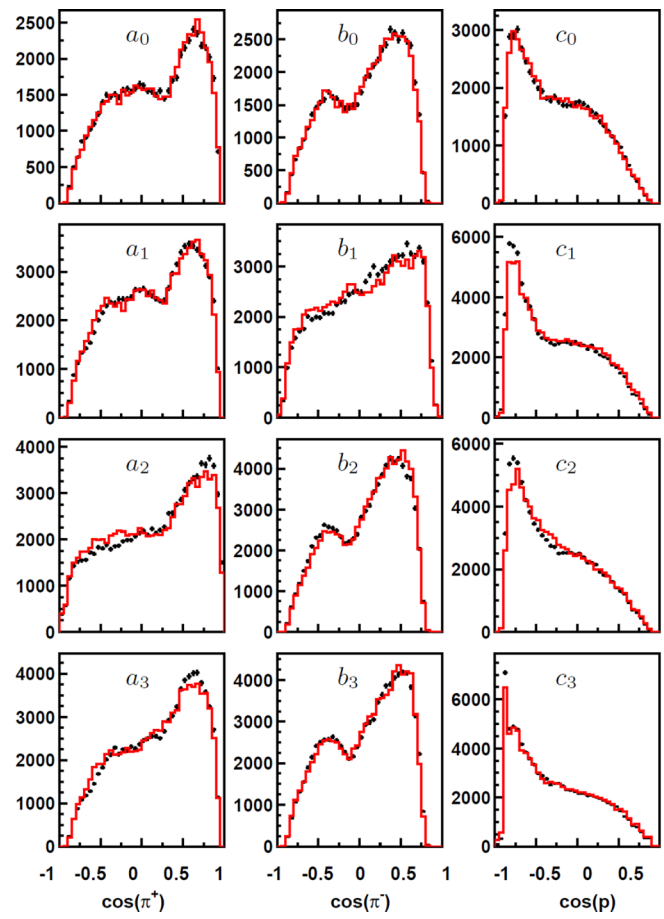

FIG. 9. The $\cos\Theta_{\pi^+}$ (a), $\cos\Theta_{\pi^-}$ (b), and $\cos\Theta_p$ (c) angular distributions in the c.m.s. for the mass range $1.9 < W < 2.1\,\text{GeV}$ and for the four topologies C_i, $i = 0, 1, 2, 3$. The distributions are not corrected for efficiency. The data are represented by crosses, our fit (in red) by the histogram.

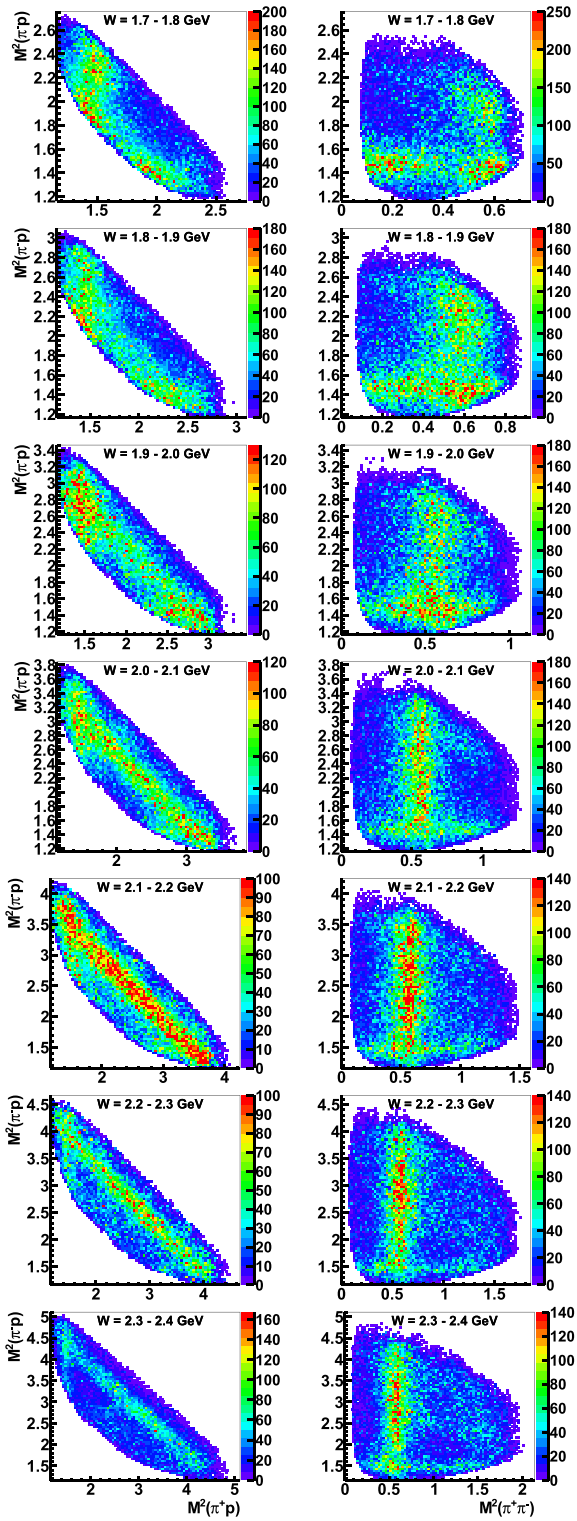

FIG. 10. Acceptance-corrected Dalitz plots $M^2_{p\pi^-}$ vs $M^2_{p\pi^+}$ and $M^2_{p\pi^+}$ vs $M^2_{\pi^+\pi^-}$. All four topologies are added. In the low-energy region, the $\Delta(1232)^{++}$ provides the most significant contribution; at high energies, $\rho(770)$ production dominates the reaction.

contributions. This is due to the Kroll-Rudermann mechanism [80]: the impinging photon can dissociate the charges within the proton, creating a $\Delta(1232)^{++}$ and a charged pion. This effect is particularly strong at low energies but persists up to the highest energies reported here. Here, it is introduced through a formalism suggested in Ref. [81].

TABLE II. Uncertainties in the cross section measurements [4]. The uncertainty in the PWA depends on the kinematic range. The total uncertainty is represented by (red) curves in Figs. 13–18 and by a range in Table IV.

Fiducial cuts	4.0%
Kinematic fitting	3.0%
Photon flux correction	1.0%
Particle detection efficiency correction	1.5%
Sum of constant uncertainties	5.3%
Three-pion contamination	0–2%

B. Mass and angular distributions of the *full data set*

Figure 11 presents the mass and angular distributions of the *full data set*. The distributions are corrected for acceptance using the JM17 model of Ref. [4]. The black curves represent the fit reported in Ref. [4] that includes the *full data set* but excludes the *event-based data sample*, while the red curves represent the new fit based solely on the *event-based data sample*, excluding the *full data set*.

Overall, the data are well reproduced, demonstrating good agreement between the *full data set* and the *event-based data sample*. However, at low energies, discrepancies are observed in the ϕ distributions, indicating that the *full data set* and the *event-based data sample* are not entirely consistent at low photon energies.

When the *full data set* is included, the fit to the polarization data yields a $\chi^2/N_{\rm data}$ of 1.33 for 2508 data points. In contrast, including the *event-based data sample* results in a $\chi^2/N_{\rm data}$ of 0.68. These results suggest that the *event-based data sample* is perfectly consistent, while the *full data set* is reasonably consistent with the polarization data [5].

C. Total cross section and excitation functions

Figure 12 presents the total cross section for the reaction $\gamma p \to p\pi^+\pi^-$. Our result is shown by bands representing the total uncertainty. It is compared to the cross section as determined by the Aachen-Berlin-Bonn-Hamburg-Heidelberg-Munich (ABBHHM) Collaboration [28] and to an earlier CLAS analysis [4]. These earlier results are given by dots and error bars. The cross section obtained by the SAPHIR Collaboration [46] is compatible. It is not shown here for the sake of clarity.

The total uncertainty in the cross section measurement contains the contributions listed in Table II. The PWA uncertainty is determined from the spread of a large number of fits. In systematic studies, we changed the fit model by adding high-mass resonances in different partial waves in the 2.2 to 2.5 GeV mass range. Furthermore, we multiplied or divided the weight of data sets in $\gamma\vec{p} \to p\pi^+\pi^-$ by a factor of 2, performed fits of the *full* $\gamma p \to p\pi^+\pi^-$ *data set* and the *event-based data sample* with all four topologies, or excluded the *full data set* or the *event-based data sample*, or used only

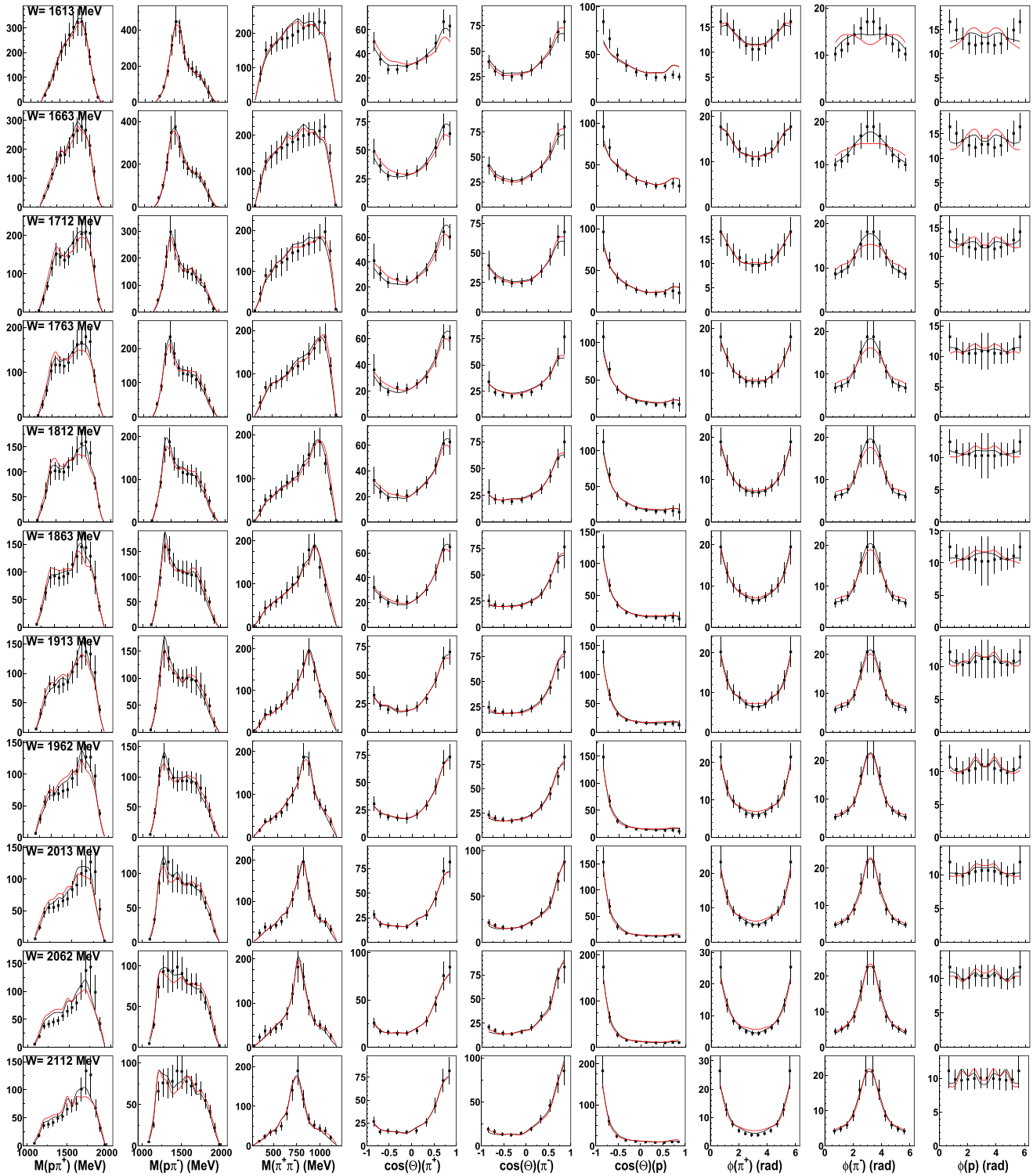

FIG. 11. Invariant mass and angular distributions for the *full data set* [4]. The black lines represent a fit to the *full data set* only, the red line a fit to the *event-based data sample*. The central value of $M_{\gamma p}$ is shown in the left-most subfigure. The bins cover a range of 25 MeV and only every second bin is shown.

one of the topologies. The largest part of the PWA uncertainty is due to the fit model; changing the weights has a minimal effect on the fit results.

Figure 12 also shows excitation functions for $\gamma p \to p\rho$, $\Delta(1232)^{++}\pi^-$, and $\Delta(1232)^0\pi^-$ and compares these to those of the SAPHIR Collaboration and to our previous results. The full nine onefold differential cross sections obtained in our previous and current analyses are consistent within entire overlapping W range in both analyses. Our earlier results on $\Delta(1232)^{++}\pi^-$ agree approximately with our new

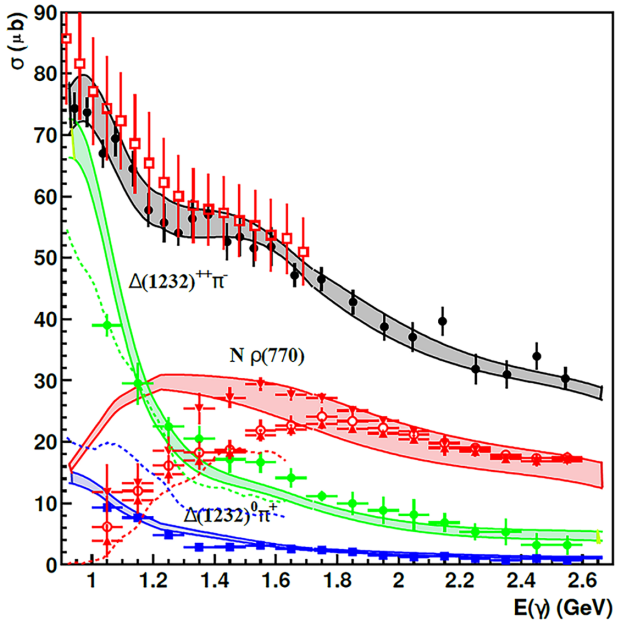

FIG. 12. The total cross section for the reaction $\gamma p \to p\pi^+\pi^-$ including different isobar contributions. Our total cross section is represented by the black-shaded band that is determined from the spread of different PWA solutions. Our result on the total cross section is compared to our earlier results covering a smaller energy range (□ [4]) and to results of the ABBHHM (• [28]) that are consistent with those from the SAPHIR Collaboration ([46]). The red, green, and blue bands represent our result on the excitation functions for $N\rho(770)$, $\Delta(1232)^{++}$, and $\Delta^0(1232)$ production, the points with error bars are the SAPHIR results, the dotted curves the results from Ref. [4]. The SAPHIR Collaboration used three fit models for the $\rho(770)$ shape, a Breit-Wigner function (○), the Söding model (▲), and the Ross-Stodolsky model (▼).

findings, in particular when some (unknown) systematic uncertainty is included for our results. Our earlier results on the $\Delta(1232)^0\pi^+$ excitation function exceed our present result and the SAPHIR result by a large factor, up to 2, while our new $\gamma p \to p\rho$ contribution significantly exceeds the earlier results. We emphasize that the purpose of Ref. [4] was the publication of cross sections and N^* photocouplings.

The SAPHIR results are consistent but more precise than those of the ABBHHM Collaboration that are not shown here. Both collaborations use three different fit models to describe $N\rho^0(770)$ production. In a first model, the $\rho^0(770)$ meson is represented by a simple nonrelativistic Breit-Wigner function. Experimentally, the $\rho^0(770)$ meson in low-energy photoproduction has an asymmetric shape. This is taken into account in the Söding model [82] of the Breit-Wigner amplitude with a Deck-type background [30]. In the Ross-Stodolsky model [83], the $\rho^0(770)$ mass distribution is multiplied by a factor $(M_\rho/M_{\pi\pi})^4$. The two $\Delta(1232)$ isobars are described by Breit-Wigner functions, their interference by an additional term. Nonresonant $N\pi\pi$ production is described by a phase-space distribution. In the BnGa approach, the three isobars shown in Fig. 12 provide the largest contributions, but other less important isobars are also admitted. Nonresonant production of $N\pi\pi$ is not needed. Interference is allowed between all amplitudes and not only for interference between $\Delta(1232)^{++}$ and $\Delta(1232)^0$. The asymmetric $\rho^0(770)$ shape is well described by a relativistic Breit-Wigner amplitude taking phase space and orbital-angular-momentum-barrier factors into account.

At low energies, the largest contribution to the cross section is provided by the Kroll-Ruderman mechanism. The $\Delta(1232)^{++}\pi^-$ contribution continues to decrease. The SAPHIR analysis finds a weak shoulder in the second and third resonance regions, which is not confirmed here. $\Delta^0(1232)\pi^+$ production is smaller by a factor 3–5, the reduction is much larger than expected if these two isobars would be dominantly produced via intermediate N^* or Δ^* resonances. We find a considerably larger cross section for the $N\rho^0(770)$ production. Note that our uncertainty is mainly due to the different solutions of the multichannel analysis, while SAPHIR gives the statistical uncertainty derived from one model. The $N\rho^0(770)$ contribution is mostly in the (20–30) μb range. The $\gamma p \to N\rho^0(770)$ cross section is nearly constant above 1.3 GeV in photon energy, pointing to diffractive scattering as the main production mechanism. The small $N\rho^0(770)$ cross section in the SAPHIR analysis, in particular at low energies, may originate from three reasons: SAPHIR fits with a large phase-space contribution and the $N\rho(770)$-$\Delta(1232)^{++}\pi^-$ interference is neglected. In the BnGa solution a notable part comes from the $N(1520)3/2^- \to N\rho$ contribution which produces a deeper slope for the $N\rho$ contribution at low energies than the t-channel exchange amplitudes.

D. $\gamma p \to N\rho^0(770)$

Differential cross sections. Figure 13 presents the differential cross sections as a function of the squared momentum transfer $-t$ to the $\rho^0(770)$ meson and as a function of the cosine of the $\rho(770)$ scattering angle $\cos\Theta_\rho^{\rm cms}$. The t dependence shows a fast exponential fall-off that is characteristic of diffractive scattering. The pion-exchange contribution is considerably smaller. Over a wide range of energies, their sum almost corresponds to the full cross section, leaving little room for N^* or Δ^* to decay to $N\rho(770)$. The $N\rho(770)$ differential cross sections in the forward direction are well described for $E_\gamma > 1.4$ GeV by Pomeron exchange only. This makes it difficult to see manifestations of the N* signals in this region. The additional intensity at backward angles reveals additional $\rho(770)$-production modes beyond Pomeron or pion exchange that suggests resonance contributions.

We fitted the t dependence below $-0.5\,\text{GeV}^2$ with an exponential function in the form $d\sigma/dt = a\exp\{-b|t|\}$. The fit values are given in Table III. The SAPHIR Collaboration finds a steeper slope and a higher yield in the forward direction. Their uncertainties are much smaller, but do not include a systematic variation of the PWA model. The ZEUS Collaboration fitted $\rho^0(770)$ production in $e\,p$ scattering [84] at $W = 55$, 65, and 84 GeV and found a mild W dependence only. In Table III, we quote the central value. At HERA energies, the cross section is considerably reduced and falls off faster with increasing momentum transfer. The $\cos\Theta_\rho^{\rm cms}$ distributions exhibit a forward rise. Note that forward $\rho^0(770)$ mesons are produced at low values for $-t$.

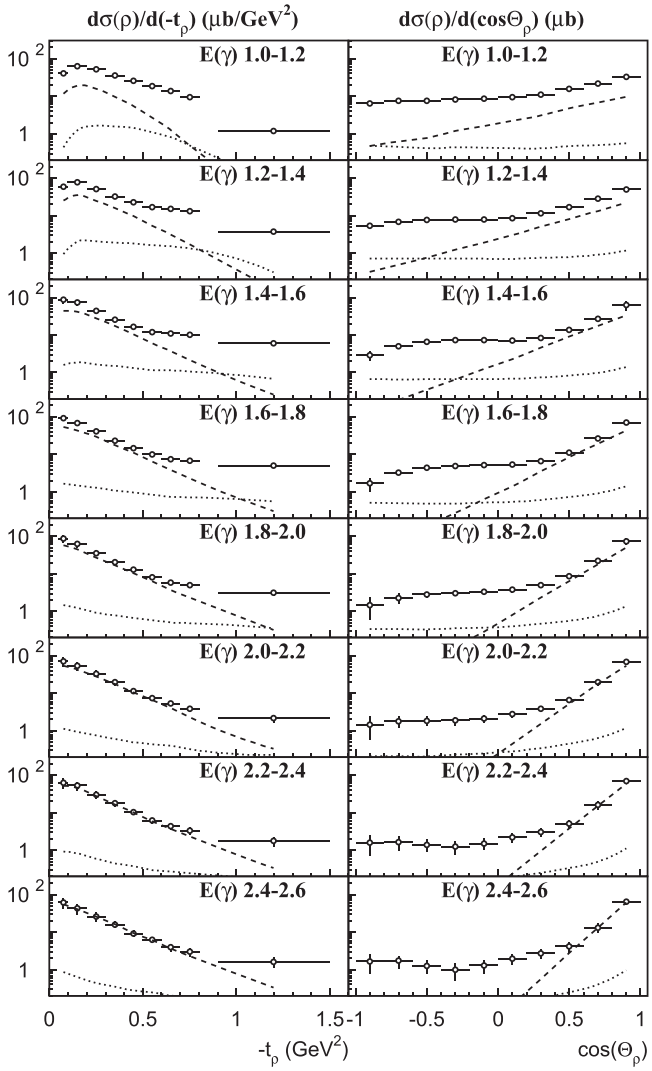

FIG. 13. Differential cross sections for $\gamma p \to N\rho^0(770)$ as a function of $-t$ (left) and cos $\Theta_\rho^{\rm cms}$ (right). The vertical and horizontal lines define the uncertainty and range of cross section measurement. The dashed curves give the contribution due to Pomeron exchange, and the dotted curves give the contribution due to pion exchange.

TABLE III. Slope of the differential cross section for photoproduction of $\rho^0(770)$ mesons from this analysis, and from the SAPHIR and ZEUS Collaborations.

	This work		SAPHIR	
E_γ GeV	a μb/GeV	b GeV^{-2}	a μb/GeV	b GeV^{-2}
1.0–1.2	115 ± 8	3.6 ± 0.6		
1.2–1.4	147 ± 8	4.3 ± 0.5		
1.4–1.6	154 ± 5	5.2 ± 0.3	170 ± 6	6.69 ± 0.17
1.6–1.8	150 ± 6	5.3 ± 0.3	175 ± 4	6.32 ± 0.10
1.8–2.0	138 ± 6	5.3 ± 0.3	164 ± 4	5.96 ± 0.09
2.0–2.2	120 ± 5	5.2 ± 0.3	136 ± 3	5.55 ± 0.08
2.2–2.4	114 ± 6	5.3 ± 0.3	121 ± 2	5.42 ± 0.08
3.2–3.9	CLAS [53]			6.4 ± 0.3
65	ZEUS [84]		12.1 ± 1.2	11.0 ± 1.0

Density matrix elements. The $\rho(770)$ meson is a vector particle. The $\rho(770)$ decay carries information on its spin alignment relative to a given axis. This information is encoded in the spin-density matrix. Its elements are extracted from angular distributions of the pions calculated in the rest system of the $\rho^0(770)$ meson. The angular distribution of its decay into two pions can be parametrized as [85]

$$W(\Theta_\pi, \phi_\pi) = \frac{3}{4\pi}\left[\frac{1}{2}(1 - \cos^2\Theta_\pi) + \frac{1}{2}(3\cos^2\Theta_\pi - 1)\rho_{00} - \rho_{1\text{-}1}\sin^2\Theta_\pi\cos 2\phi_\pi - \sqrt{2}\,\mathrm{Re}\,\rho_{10}\sin 2\Theta_\pi\cos\phi_\pi\right]. \quad (6)$$

These angular distributions depend on the orientation of the axis in the rest system of the two-pion system. For $\rho^0(770)$ meson production two systems are considered: the helicity system, where the z axis is directed along the momentum of the final-state nucleon recoiling against the $\rho^0(770)$ meson, and the Gottfried-Jackson system, where the z axis is directed along the photon beam axis. In both systems the reaction plane is defined by the beam momentum and the proton momentum (see Fig. 6). The elements of the density matrix reveal flips of the spin relative to the direction of the $\rho^0(770)$ momentum in the helicity frame or to the direction of the photon in the Gottfried-Jackson frame. For helicity conservation in a given frame, the corresponding three spin-density matrix elements vanish. Figure 14 shows the spin-density matrix elements for photoproduction of $\rho^0(770)$ mesons as a function of $-t$ in the Gottfried-Jackson frame; Fig. 15 is the same in the helicity frame. In the helicity frame, vanishing spin-density matrix elements would be expected if photoproduction of $\rho(770)$ mesons were fully dominated by diffractive scattering where the incoming photons virtually convert into a vector meson that scatters off the proton via natural (e.g., Pomeron) or unnatural (e.g., pion) parity exchange. Diffractive scattering is not the only process contributing to $\rho(770)$ production. With increasing energy, vanishing spin-density matrix elements in the helicity frame lead to a sin 2Θ distribution in the Gottfried-Jackson frame that can be recognized in the experimental distributions. This behavior is expected for diffractive scattering: the photon virtually converts to a $\rho^0(770)$ mesons that scatters off the proton by Pomeron or pion exchange keeping the orientation of its spin.

E. $\gamma p \to \Delta(1232)^{++}\pi^-$

Differential cross sections. Figure 16 shows the differential cross section for the $\Delta(1232)^{++}$ as a function of cos Θ_{π^-}, where Θ_{π^-} is the c.m.s. angle. The direct production of $\Delta(1232)^{++}$ plays a very significant role, pion exchange is less important. Significant room is left for N^* and Δ^* resonances decaying into $\Delta(1232)\pi$.

Spin-density matrix elements. In the case of the production of a baryon with spin $3/2^+$, the elements of the density matrix can be extracted from the angular dependence of π^+ calculated in the rest frame of the resonance

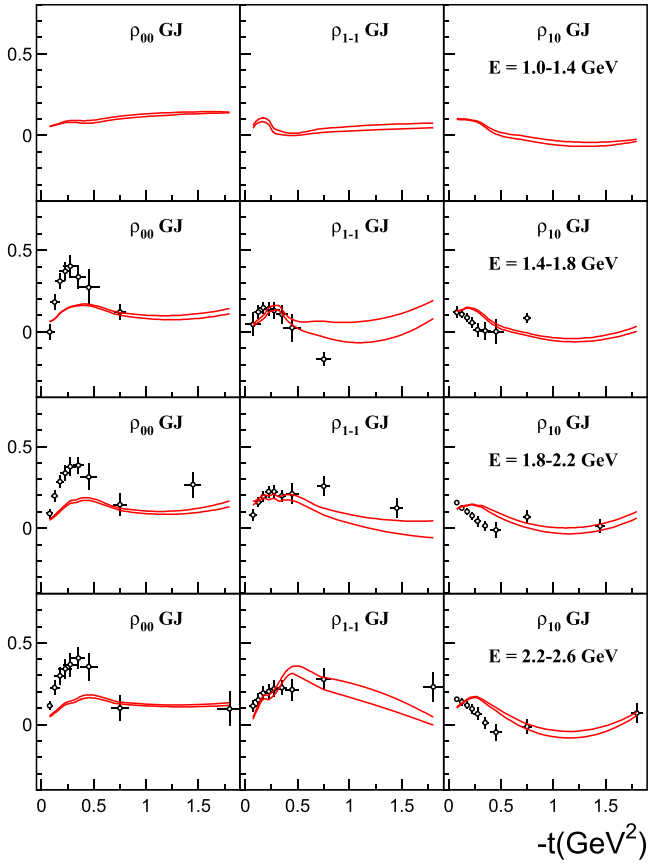

FIG. 14. The spin-density matrix elements for the decay of the $\rho^0(770)$ meson as a function of the (squared) transferred momentum calculated in the Gottfried-Jackson frame. The two red lines show the range of the spin-density matrix elements calculated from the set of the final solutions. The data points with error bars show the result obtained by the SAPHIR Collaboration [46].

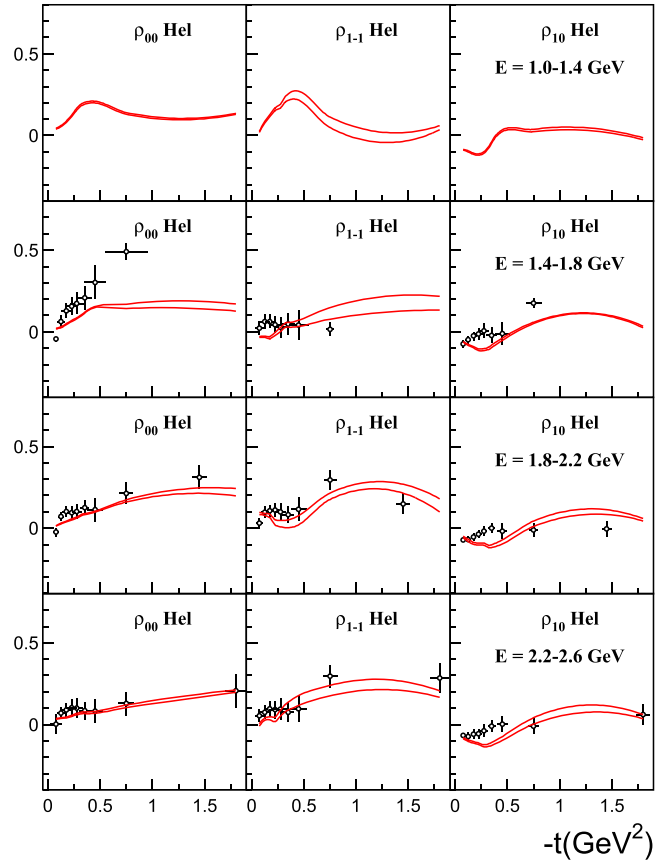

FIG. 15. The spin-density matrix elements for the $\rho^0(770)$ meson decay in dependence on the momentum transferred squared calculated in the helicity frame. The red lines show the range of the spin-density matrix elements calculated from the set of the final solutions. The data points with error bars show the result obtained by the SAPHIR Collaboration [46].

system [86]:

$$W(\Theta_\pi,\phi_\pi) = \frac{1}{4\pi}\Big[\frac{1}{2}(1+3\cos^2\Theta_\pi) + 2(1-3\cos^2\Theta_\pi) \times \rho_{\frac{3}{2}\frac{3}{2}} - 2\sqrt{3}\,\mathrm{Re}\rho_{\frac{3}{2}-\frac{1}{2}}\sin^2\Theta_\pi\cos 2\phi_\pi - 2\sqrt{3}\,\mathrm{Re}\rho_{\frac{3}{2}\frac{1}{2}}\sin 2\Theta_\pi\cos\phi_\pi\Big]. \quad (7)$$

The elements of the spin-density matrix were extracted in the helicity system where the reaction plane is defined by the beam and π^- momenta and the z axis is directed along the π^- momentum. The elements presented in Fig. 17 show very significant structures that support the evidence for the production of decays N^* and $\Delta^* \to \Delta(1232)\pi$.

F. $\gamma p \to \Delta(1232)^0\pi^+$

Differential cross sections. The differential cross section for $\gamma p \to \Delta^0(1232)\pi^+$ (see Fig. 18) is considerably smaller than the one for $\Delta(1232)^{++}$ production. At low photon energies, there is little backward-forward asymmetry. Only at higher energies does pion exchange play a significant role leading to fast forward π^+ mesons.

Spin-density matrix elements. The spin-density matrix elements extracted in the helicity system for $\gamma p \to \Delta(1232)^0\pi^+$ in Fig. 19 also show significant structures, again likely due to production of N^* and $\Delta^* \to \Delta(1232)\pi$ decays.

V. BRANCHING RATIOS FOR THE DECAYS N^* AND $\Delta^* \to N\rho(770)$

The differential cross sections for $\rho^0(770)$ meson production as a function of the squared momentum transfer $-t$ (see Fig. 13) show some additional intensity at backward angles suggesting resonance contributions. In fact, coupled-channel analysis requires significant contributions from N^* and $\Delta^* \to N\rho(770)$. The resulting branching ratios are presented in Table IV. The branching ratios are calculated by integration over the ρ line shape and the width of the resonance under study; see Ref. [87].

In most cases, the values are compatible with those given in the Review of Particle Physics (RPP) [88] even though

TABLE IV. Branching ratios in % for decays of N^* and Δ^* resonances into $N\rho$. The results are obtained by integration over the ρ width and over the width of the resonance. The small numbers are estimates of the Particle Data Group [88]. These branching ratios are mostly determined without integration.

		$(N\rho)_{\rm tot}$	$N\rho$		
			$S=\frac{1}{2}$	$S=\frac{3}{2}$	
				$L<J$	$L>J$
$N(1440)$	$\frac{1}{2}^+$	18 ± 6 17–50	9 ± 4		9 ± 4 $6-27$
$N(1520)$	$\frac{3}{2}^-$	28 ± 4 10–16	4 ± 3 0.2–0.4	24 ± 3 10–16	<1
$N(1535)$	$\frac{1}{2}^-$	9 ± 4 2–17	7 ± 3 2–16		2 ± 2 <1
$N(1650)$	$\frac{1}{2}^-$	17 ± 6 12–22	12 ± 5 <4		5 ± 3 12–18
$N(1675)$	$\frac{5}{2}^-$	30 ± 8 0.1–0.9	20 ± 7 <0.2	10 ± 5 0.1–0.7	<1
$N(1680)$	$\frac{5}{2}^+$	10 ± 5 8–11	<1	9 ± 4 6–8	<1 2–3
$N(1700)$	$\frac{3}{2}^-$	21 ± 9 32–44	5 ± 3	<1 32–44	16 ± 8
$N(1710)$	$\frac{1}{2}^+$	17 ± 4 11–23	6 ± 2 11–23		11 ± 3
$N(1720)$	$\frac{3}{2}^+$	29 ± 8 1–2	12 ± 5 1–2	17 ± 6	<1
$N(1860)$	$\frac{5}{2}^+$	54 ± 16 <8.6	16 ± 9	13 ± 5 <8.5	25 ± 12 <0.1
$N(1875)$	$\frac{3}{2}^-$	12 ± 4	4 ± 2	8 ± 3 36–56	<1
$N(1880)$	$\frac{1}{2}^+$	28 ± 7 19–45	20 ± 6 19–45		8 ± 3
$N(1895)$	$\frac{1}{2}^-$	43 ± 25 14–50	18 ± 5 <18		25 ± 14 $14-32$
$N(1900)$	$\frac{3}{2}^+$	46 ± 17 25–40	7 ± 4 25–40	9 ± 3	30 ± 12
$N(1990)$	$\frac{7}{2}^+$	10 ± 5	8 ± 4	2 ± 2	<1
$N(2000)$	$\frac{5}{2}^+$	15 ± 4	8 ± 3	7 ± 3	<1
$N(2060)$	$\frac{5}{2}^-$	28 ± 11 5–33	24 ± 10 <10	4 ± 4 5–23	<1
$N(2100)$	$\frac{1}{2}^+$	17 ± 7 35–70	12 ± 6 35–70		5 ± 3
$N(2120)$	$\frac{3}{2}^-$	28 ± 6	4 ± 2	19 ± 5 <3	5 ± 3
$N(2190)$	$\frac{7}{2}^-$	9 ± 7	<1	8 ± 7 <11	<1
$\Delta(1600)$	$\frac{3}{2}^+$	7 ± 4	2 ± 2	5 ± 3	<1
$\Delta(1620)$	$\frac{1}{2}^-$	52 ± 17 23–32	30 ± 12 23–32		22 ± 12 <0.04
$\Delta(1700)$	$\frac{3}{2}^-$	14 ± 4	<1	13 ± 4 22–32	<1
$\Delta(1750)$	$\frac{1}{2}^+$	27 ± 13	17 ± 10		10 ± 8
$\Delta(1900)$	$\frac{1}{2}^-$	38 ± 13 22–60	18 ± 8 11–35		20 ± 10 11–25
$\Delta(1905)$	$\frac{5}{2}^+$	26 ± 10	<1	25 ± 10	<1

TABLE IV. (*Continued.*)

		$(N\rho)_{\rm tot}$	$N\rho$		
			$S=\frac{1}{2}$	$S=\frac{3}{2}$	
				$L<J$	$L>J$
				17–35	
$\Delta(1910)$	$\frac{1}{2}^+$	10 ± 4	5 ± 3		5 ± 3
$\Delta(1920)$	$\frac{3}{2}^+$	57 ± 9	8 ± 4	14 ± 5	35 ± 6
$\Delta(1930)$	$\frac{5}{2}^-$	33 ± 8	3 ± 2	<1	30 ± 8
$\Delta(1950)$	$\frac{7}{2}^+$	10 ± 5	10 ± 5	<1	<1
$\Delta(2200)$	$\frac{7}{2}^-$	36 ± 14	21 ± 12	<1	15 ± 9

some branching ratios differ significantly. This may be not too surprising: the range of values listed in the RPP often represents just the statistical uncertainty in an analysis. An

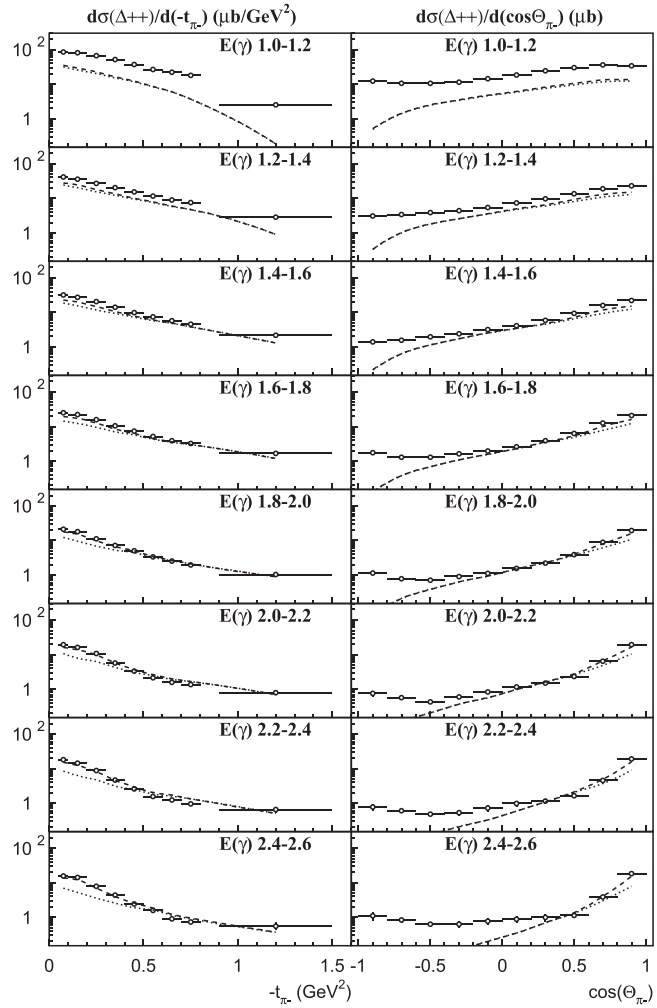

FIG. 16. Differential cross sections for $\gamma p \to \Delta(1232)^{++}\pi^-$ as a function of $-t$ (left) and $\cos\Theta_\rho^{\rm cms}$ (right). The vertical and horizontal lines define uncertainty and range of cross section measurement. The dotted curve represents the Kroll-Rudermann contribution, the dashed curve the pion-exchange contribution.

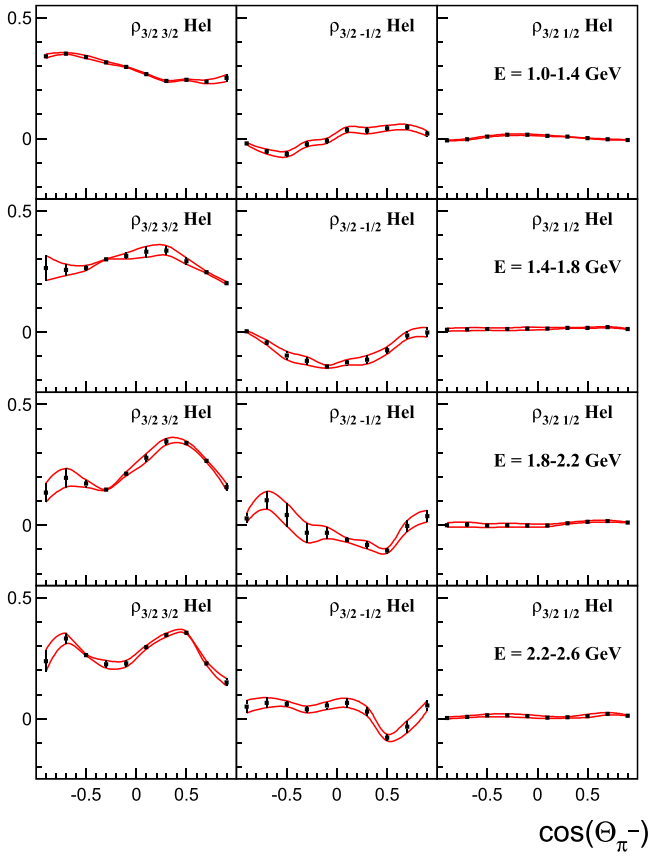

FIG. 17. The spin-density matrix elements for the $\Delta(1232)^{++}$ decay as a function of $\cos\Theta_{\pi^-}$ calculated in the helicity frame. The (red) curves show the range of the spin-density matrix elements calculated from the set of the final solutions.

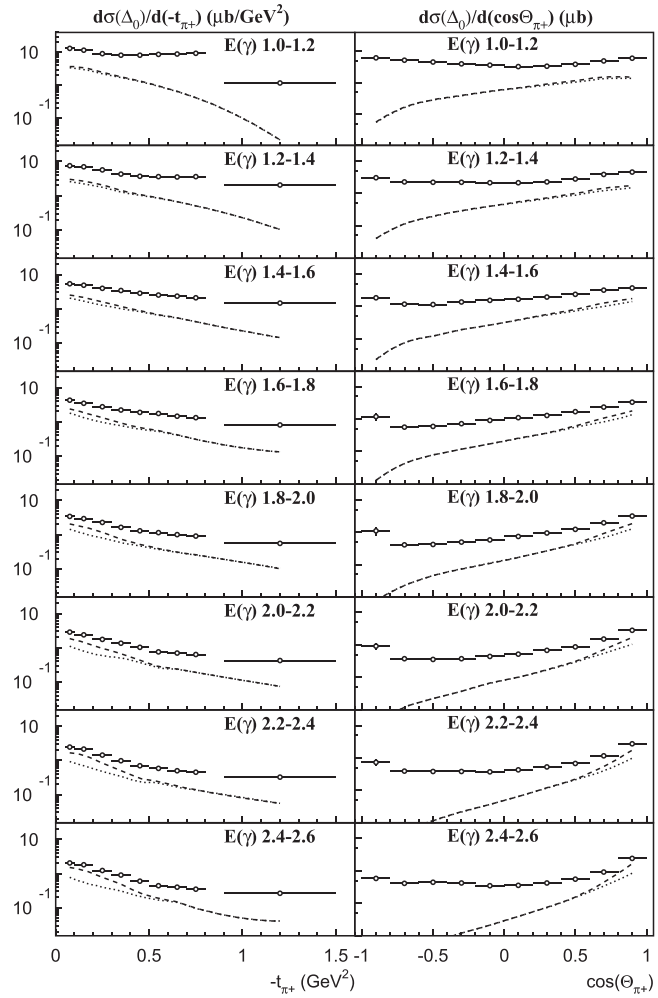

FIG. 18. Differential cross sections for $\gamma p \to \Delta(1232)^0\pi^+$ as a function of $-t$ (left) and $\cos\Theta_\rho^{\rm cms}$ (right). The uncertainties are smaller than the open circles; the horizontal lines define the range of cross section measurement. The dashed curves gives the pion-exchange contribution and the dotted curves shows the Born term.

extreme example is the decay $N(1720)\frac{3}{2}^+ \to N\rho$: Shrestha and Manley [89] give a branching ratio $N(1720)\frac{3}{2}^+ \to N\rho, S = \frac{1}{2}, P$ wave of $(1.4 \pm 0.5)\%$ that defines the RPP entry. The measurement of Vrana *et al.* [90], giving $(91 \pm 1)\%$, is not used to define a range. Contributions from $N\rho$ decays with N and ρ spins aligned to $S = 3/2$ were not tested in either analysis. For $N(1875)\frac{3}{2}^- \to N\rho$, Hunt and Manley [91] report a branching ratio $N(1875)\frac{3}{2}^- \to N\rho, S = \frac{3}{2}, S$ wave of $(46 \pm 10)\%$ that defines the RPP entry; the values from Shrestha and Manley [89] and Vrana *et al.* [90], who find <5% and $(6 \pm 6)\%$, are not used. The branching ratios $N(1675)\frac{5}{2}^-$ and $N(2120)\frac{3}{2}^- \to N\rho$, where large discrepancies are seen, have so far been determined only by Hunt and Manley [91]; in the analyses [89,90] there was no need to introduce these contributions. The large discrepancies evidence the limitations of the database that have existed so far and the difficulty of the analyses.

VI. SUMMARY

We studied the reaction $\gamma p \to p\pi^+\pi^-$ for photon energies from 0.7 to 2.4 GeV with the CLAS detector at Jefferson Lab. The full data set of 400 million reconstructed events is included in the form of invariant mass and angular distributions, and a subsample of nearly 2 million events is used in an event-based likelihood fit. This is the first analysis in which an event-based likelihood fit is made on the reaction $\gamma p \to p\pi^+\pi^-$.

Events with the three particles reconstructed and events with a missing π^+, π^-, or proton are analyzed. The full data set and the subsample are interpreted within the BnGa coupled-channel analysis. The analysis reveals strong $p\rho^0(770)$ and $\Delta(1232)^{++}\pi^-$ production and weaker production of $\Delta(1232)^0\pi^+$. Differential cross section and spin-density matrix elements are presented. The production of $\rho^0(770)$ mesons can be assigned largely to diffractive scattering via exchange of Pomeron and pion trajectories. $\Delta(1232)^{++}$ production is strong due to the Kroll-Rudermann mechanism. Deviations of the behavior expected for these dominant contributions point at a production via intermediate resonances decaying into $N\rho(770)$ and $\Delta(1232)\pi$.

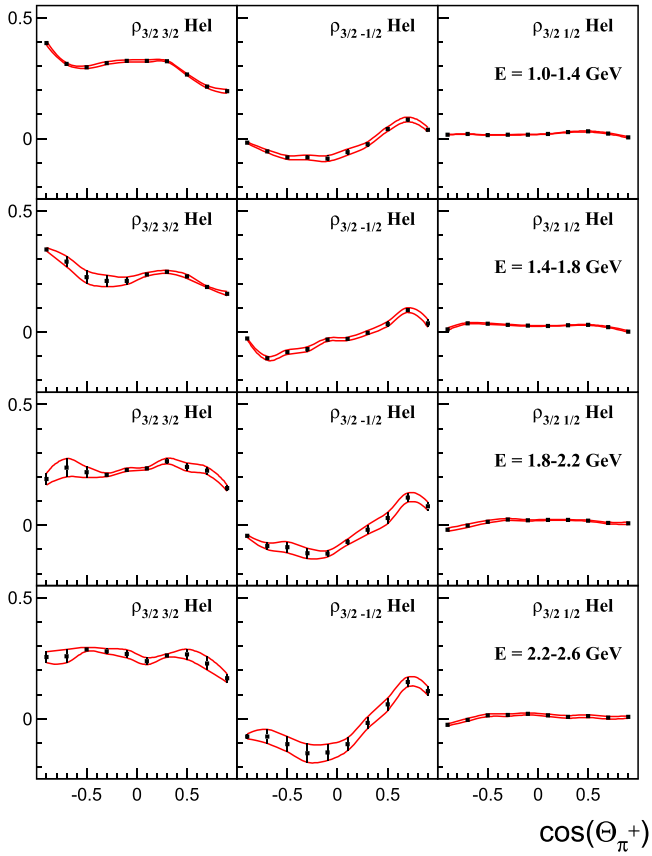

FIG. 19. The spin-density matrix elements for the $\Delta(1232)^0$ decay as a function of $\cos\Theta_{\pi^+}$ calculated in the helicity frame. The two red lines show the range of the spin-density matrix elements calculated from the set of the final solutions.

The BnGa coupled-channel analysis provides masses, widths, and branching ratios for decays of the contributing resonances into a large number of final states, including intermediate resonances. Here, we have reported the branching ratios for $N\rho$ decays that are uniquely determined by the CLAS data on $\gamma p \to p\pi^+\pi^-$. In particular, the *event-based data sample* plays a decisive role for the results presented here.

ACKNOWLEDGMENTS

The authors thank the technical staff at Jefferson Lab and at all the participating institutions for their invaluable contributions to the success of the experiment. This material is based on work supported by the U.S. Department of Energy, Office of Science, Office of Nuclear Physics, under Contract No. DE-AC05-06OR23177. The work was supported by the Deutsche Forschungsgemeinschaft (SFB/TR110), the U.S. Department of Energy (DE-AC05-06OR23177, DE-FG02-92ER40735), the Russian Science Foundation (RSF 24-22-00322), the U.S. National Science Foundation, the State Committee of Science of Republic of Armenia, the Chilean Comisión Nacional de Investigación Cientifica y Tecnológica (CONICYT), the Italian Istituto Nazionale di Fisica Nucleare, the French Centre National de la Recherche Scientifique, the French Commissariat a l'Energie Atomique, the Scottish Universities Physics Alliance (SUPA), the United Kingdom's Science and Technology Facilities Council, and the National Research Foundation of Korea.

DATA AVAILABILITY

The data supporting this study's findings are available within the article.

[1] F. D. Aaron *et al.* (H1 Collaboration), Diffractive Electroproduction of $\rho(770)$ and ϕ mesons at HERA, J. High Energy Phys. 05 (2010) 032.
[2] F. Gross, E. Klempt *et al.*, 50 Years of quantum chromodynamics, Eur. Phys. J. C **83**, 1125 (2023).
[3] D. Lüke and P. Söding, Multiple pion photoproduction in the *s*-channel resonance region, in S*ymposium on Meson-, Photo-, and Electro-production at Low and Intermediate Energies*, Springer Tracts in Modern Physics Vol. 59 (Springer, Berlin, 1971), p. 39.
[4] E. Golovatch *et al.* (CLAS Collaboration), First results on nucleon resonance photocouplings from the $\gamma p \to \pi^+\pi^- p$ reaction, Phys. Lett. B **788**, 371 (2019).
[5] P. Roy *et al.* (CLAS Collaboration), Measurement of (double-)polarization observables in the photoproduction of $\pi^+\pi^-$ meson pairs off the proton using CLAS at Jefferson Laboratory (unpublished).
[6] A. V. Sarantsev *et al.*, Decays of N and Δ resonances into $p\pi^+\pi^-$ (unpublished).
[7] V. I. Mokeev *et al.*, First results on nucleon resonance electroexcitation amplitudes from $ep \to e'\pi^+\pi^- p'$ cross sections at $W = 1.4$–1.7 GeV and $Q^2 = 2.0$–5.0 GeV^2, Phys. Rev. C **108**, 025204 (2023).
[8] V. D. Burkert, Nucleon resonances and transition form factors, in Ref. [2], arXiv:2212.08980.
[9] J. Kirz, J. Schwartz, and R. D. Tripp, Reaction $\pi^- p \to \pi^-\pi^+ n$ from 360 to 800 MeV, Phys. Rev. **130**, 2481 (1963).
[10] D. H. Saxon, J. H. Mulvey, and W. Chinowsky, $\pi^- p$ reactions at 456, 505, and 552 MeV/c, Phys. Rev. D **2**, 1790 (1970).
[11] M. De Beer *et al.*, Partial wave analysis of the reaction $\pi N \to N\pi\pi$ below 1 GeV: (I) $\pi^- p$ inelastic interactions, Nucl. Phys. B **12**, 599 (1969).
[12] M. De Beer *et al.*, Partial wave analysis of the reaction $\pi N \to N\pi\pi$ below 1 GeV: (II) $\pi^+ p$ inelastic interactions, Nucl. Phys. B **12**, 617 (1969).
[13] A. D. Brody *et al.*, Experimental results on the reactions $\pi^- p \to \pi\pi N$ in the c.m. energy range 1400–2000 MeV, Phys. Rev. D **4**, 2693 (1971); **5**, 2899(E) (1972).
[14] J. Dolbeau, M. Neveu, F. A. Triantis and C. Coutures, Experimental results on $\pi^- p$ interactions in the cm energy range 1.50–1.74 GeV, Nucl. Phys. B **78**, 233 (1974).
[15] K. W. J. Barnham *et al.*, An isobar model partial wave analysis of three-body final states in $\pi^+ p$ interactions from threshold to 1700 MeV c.m. energy, Nucl. Phys. B **168**, 243 (1980).

[16] A. V. Kravtsov *et al.*, Measurement of the $\pi^- n \to \pi^- \pi^- p$ cross-sections near the threshold, Nucl. Phys. B **134**, 413 (1978).

[17] A. A. Belkov *et al.*, The investigation of the $\pi^- p \to \pi^0 \pi^0 n$ reaction near the threshold, Sov. J. Nucl. Phys. **31**, 96 (1980).

[18] C. W. Bjork *et al.*, Measurement of $\pi^- p \to \pi^+ \pi^- n$ near threshold and chiral symmetry breaking, Phys. Rev. Lett. **44**, 62 (1980).

[19] R. Aaron, R. A. Arndt, J. B. Cammarata, D. A. Dicus, and V. L. Teplitz, Analysis of $\pi^- p \to \pi^+ \pi^- n$ below 1400 MeV and chiral symmetry breaking, Phys. Rev. Lett. **44**, 66 (1980).

[20] G. Kernel *et al.* (OMICRON Collaboration), Cross-section measurement of $\pi^- p \to \pi^- \pi^+ n$ reaction near threshold, Phys. Lett. B **216**, 244 (1989).

[21] G. Kernel *et al.* (OMICRON Collaboration), Measurement of $\pi^- p \to \pi^- p \pi^0$ reaction near threshold and breaking of chiral symmetry, Phys. Lett. B **225**, 198 (1989).

[22] G. Kernel *et al.* (OMICRON Collaboration), Measurement of the reaction $\pi^+ p \to \pi^+ \pi^+ n$ near threshold, Z. Phys. C **48**, 201 (1990).

[23] M. E. Sevior, R. A. Arndt, J. B. Cammarata, D. A. Dicus, and V. L. Teplitz, Measurement of the $H(\pi^+, \pi^+\pi^+)n$ cross-section very near threshold and chiral symmetry, Phys. Rev. Lett. **66**, 2569 (1991).

[24] J. Lowe *et al.*, $\pi^- p \to \pi^0 \pi^0 n$ near threshold and chiral symmetry breaking, Phys. Rev. C **44**, 956 (1991).

[25] S. Prakhov *et al.* (Crystal Ball Collaboration), Measurement of $\pi^- p \to \pi^0 \pi^0 n$ from threshold to $p_{\pi^-} = 750\,\mathrm{MeV}/c$, Phys. Rev. C **69**, 045202 (2004).

[26] J. Adamczewski-Musch *et al.* (HADES Collaboration), Two-pion production in the second resonance region in $\pi^- p$ collisions with the High-Acceptance Di-Electron Spectrometer (HADES), Phys. Rev. C **102**, 024001 (2020).

[27] H. R. Crouch *et al.* (Cambridge Bubble Chamber Group), Production of the $N^*(1238)$ nucleon isobar by photons of energy up to 6 BeV, Phys. Rev. **163**, 1510 (1967).

[28] R. Erbe *et al.* (Aachen–Berlin–Bonn–Hamburg–Heidelberg–München Collaboration), Photoproduction of meson and baryon resonances at energies up to 5.8 GeV, Phys. Rev. **175**, 1669 (1968).

[29] R. Erbe *et al.* (Aachen–Berlin–Bonn–Hamburg–Heidelberg–München Collaboration), Multipion and strange-particle photoproduction on protons at energies up to 5.8 GeV, Phys. Rev. **188**, 2060 (1969).

[30] J. Ballam *et al.*, Bubble chamber study of photoproduction by 2.8 and 4.7 GeV polarized photons. I. Cross-section determinations and production of ρ^0 and Δ^{++} in the reaction $\gamma p \to p\pi^+\pi^-$, Phys. Rev. D **5**, 545 (1972).

[31] J. Ballam *et al.*, Study of high-energy photoproduction with positron annihilation radiation: I. Three prong events, Phys. Rev. D **5**, 15 (1972).

[32] A. Braghieri *et al.*, Total cross-section measurement for the three double pion production channels on the proton, Phys. Lett. B **363**, 46 (1995).

[33] F. Harter *et al.*, Two neutral pion photoproduction off the proton between threshold and 800 MeV, Phys. Lett. B **401**, 229 (1997).

[34] M. Wolf *et al.*, Photoproduction of neutral pion pairs from the proton, Eur. Phys. J. A **9**, 5 (2000).

[35] J. Ahrens *et al.* (GDH and A2 Collaborations), Intermediate resonance excitation in the $\gamma p \to p\, 2\pi^0$ reaction, Phys. Lett. B **624**, 173 (2005).

[36] F. Zehr *et al.* (Crystal Ball at MAMI, TAPS, and A2 Collaborations), Photoproduction of $\pi^0\pi^0$ and $\pi^0\pi^\pm$ pairs off the proton from threshold to the second resonance region, Eur. Phys. J. A **48**, 98 (2012).

[37] J. Ahrens *et al.* (GDH and A2 Collaborations), First measurement of the helicity dependence for the $\gamma p \to \pi^+\pi^- p$ reaction, Eur. Phys. J. A **34**, 11 (2007).

[38] M. Kotulla *et al.*, Double π^0 photoproduction off the proton at threshold, Phys. Lett. B **578**, 63 (2004).

[39] V. L. Kashevarov *et al.* (Crystal Ball at MAMI, TAPS, and A2 Collaborations), Experimental study of the $\gamma p \to \pi^0\pi^0 p$ reaction system with the Crystal Ball/TAPS detector system at the Mainz Microtron, Phys. Rev. C **85**, 064610 (2012).

[40] M. Dieterle *et al.* (A2 Collaboration), Photoproduction of π^0 -pairs off protons and off neutrons, Eur. Phys. J. A **51**, 142 (2015).

[41] M. Dieterle *et al.* (A2 Collaboration), Helicity-dependent cross sections for the photoproduction of π^0 pairs from nucleons, Phys. Rev. Lett. **125**, 062001 (2020).

[42] S. Garni *et al.* (A2 Collaboration), Target and beam-target asymmetries for the $\gamma p \to \pi^0\pi^0 p$ reaction, arXiv:2207.14079.

[43] Y. Assafiri *et al.* (GRAAL Collaboration), Double π^0 photoproduction on the proton at GRAAL, Phys. Rev. Lett. **90**, 222001 (2003).

[44] J. Ajaka *et al.* (GRAAL Collaboration), Double π^0 photoproduction on the neutron at GRAAL, Phys. Lett. B **651**, 108 (2007).

[45] H. Kohri *et al.* (LEPS Collaboration), Differential cross section and photon-beam asymmetry for the $\gamma p \to \pi^- \Delta^{++}(1232)$ reaction at forward π^- angles for $E_\gamma = 1.5$–2.95 GeV, Phys. Rev. Lett. **120**, 202004 (2018).

[46] C. Wu *et al.* (SAPHIR Collaboration), Photoproduction of ρ^0 mesons and Δ-baryons in the reaction $\gamma p \to p\pi^+\pi^-$ at energies up to $\sqrt{s} = 2.6$ GeV, Eur. Phys. J. A **23**, 317 (2005).

[47] U. Thoma *et al.* (CBELSA/TAPS Collaboration), N^* and Δ^* decays into $N\pi^0\pi^0$, Phys. Lett. B **659**, 87 (2008).

[48] A. V. Sarantsev *et al.* (CBELSA/TAPS Collaboration), New results on the Roper resonance and the P_{11} partial wave, Phys. Lett. B **659**, 94 (2008).

[49] V. Sokhoyan *et al.* (CBELSA/TAPS Collaboration), High-statistics study of the reaction $\gamma p \to 2\pi^0$, Eur. Phys. J. A **51**, 95 (2015) [**51**, 187(E) (2015)].

[50] V. Sokhoyan *et al.* (CBELSA/TAPS Collaboration), Data on I^s and I^c in $\vec{\gamma} \to p\pi^0\pi^0$ reveal cascade decays of $N(1900)$ via $N(1520)\pi$, Phys. Lett. B **746**, 127 (2015).

[51] A. Thiel *et al.* (CBELSA/TAPS Collaboration), Three-body nature of N^* and Δ^* resonances from sequential decay chains, Phys. Rev. Lett. **114**, 091803 (2015).

[52] T. Seifen *et al.* (CBELSA/TAPS Collaboration), Polarization observables in double neutral pion photoproduction, arXiv:2207.01981.

[53] M. Battaglieri *et al.* (CLAS Collaboration), Photoproduction of the ρ^0 meson on the proton at large momentum transfer, Phys. Rev. Lett. **87**, 172002 (2001).

[54] S. Strauch *et al.* (CLAS Collaboration), Beam-helicity asymmetries in double-charged-pion photoproduction on the proton, Phys. Rev. Lett. **95**, 162003 (2005).

[55] M. Battaglieri *et al.* (CLAS Collaboration), Photoproduction of $\pi^+\pi^-$ meson pairs on the proton, Phys. Rev. D **80**, 072005 (2009).

[56] V. I. Mokeev *et al.*, Evidence for the $N'(1720)3/2^+$ nucleon resonance from combined studies of CLAS $\pi^+\pi^- p$ photo- and electroproduction data, Phys. Lett. B **805**, 135457 (2020).

[57] S. Adhikari *et al.* (GlueX Collaboration), Measurement of spin-density matrix elements in $\rho(770)$ production with a linearly polarized photon beam at $E_\gamma = 8.2$–8.8 GeV, Phys. Rev. C **108**, 055204 (2023).

[58] F. Afzal *et al.* (GlueX Collaboration), Measurement of Spin-Density Matrix Elements in $\Delta(1232)^{++}$ photoproduction, arXiv:2406.12829.

[59] B. A. Mecking *et al.*, The CEBAF Large Acceptance Spectrometer (CLAS), Nucl. Instrum. Methods Phys. Res. Sect. A **503**, 513 (2003).

[60] D. I. Sober *et al.*, The bremsstrahlung tagged photon beam in Hall B at JLab, Nucl. Instrum. Methods Phys. Res. Sect. A **440**, 263 (2000).

[61] S. Stepanyan *et al.*, Energy calibration of the JLab bremsstrahlung tagging system, Nucl. Instrum. Methods Phys. Res. Sect. A **572**, 654 (2007).

[62] J. Ball and E. Pasyuk, Photon flux determination through sampling of "out-of-time" hits with the Hall B photon tagger, CLAS-NOTE 2005-002 (2005), https://misportal.jlab.org/ul/Physics/Hall-B/clas/viewFile.cfm/2005-002.pdf?documentId=24.

[63] M. Williams, Measurement of the differential cross section and matrix elements along with a partial wave analysis for $\gamma p \to p\omega$ using CLAS at Jefferson Lab, Ph.D. thesis, Carnegie Mellon University, 2007 (unpublished).

[64] R. Bradford and R. A. Schumacher, Liquid hydrogen density in the G1C CLAS cryotarget, CLAS-NOTE 2002-003 (2002), https://www.jlab.org/Hall-B/notes/clas_notes02/02-003.pdf.

[65] M. D. Mestayer *et al.*, The CLAS drift chamber system, Nucl. Instrum. Methods Phys. Res. Sect. A **449**, 81 (2000).

[66] Y. G. Sharabian *et al.*, A new highly segmented start counter for the CLAS detector, Nucl. Instrum. Methods Phys. Res. Sect. A **556**, 246 (2006).

[67] E. S. Smith *et al.*, The time-of-flight system for CLAS, Nucl. Instrum. Methods Phys. Res. Sect. A **432**, 265 (1999).

[68] M. Amarian *et al.*, The CLAS forward electromagnetic calorimeter, Nucl. Instrum. Methods Phys. Res. Sect. A **460**, 239 (2001).

[69] E. Golovatch, Cross section of the reaction $\gamma p \to p\pi^+\pi^-$ from the G11A run period, CLAS analysis note, 2016 (unpublished).

[70] M. Holtrop, CLAS GEANT Simulation, http://nuclear.unh.edu/~maurik/gsim_info.shtml.

[71] I. G. Aznauryan, V. D. Burkert, G. V. Fedotov, B. S. Ishkhanov, and V. I. Mokeev, Electroexcitation of nucleon resonances at $Q^2 = 0.65(\mathrm{GeV}/c)^2$ from a combined analysis of single- and double-pion electroproduction data, Phys. Rev. C **72**, 045201 (2005).

[72] M. Ripani *et al.*, A Phenomenological description of $\pi^-\Delta^{++}$ photo- and electroproduction in nucleon resonance region, Nucl. Phys. A **672**, 220 (2000).

[73] E. Pasyuk, Energy loss corrections for charged particles in CLAS, CLAS-NOTE 2007-016 (2007), https://misportal.jlab.org/ul/Physics/Hall-B/clas/viewFile.cfm/2007-016.pdf?documentId=423.

[74] M. Williams and C. A. Meyer, Kinematic fitting with CLAS, CLAS-NOTE 2003-017 (2003), https://www.jlab.org/Hall-B/notes/clas_notes03/03-017.pdf.

[75] W. Briscoe, M. Doering, H. Haberzettl, I. Strakovsky, and R. Workman, INS DAC Services [SAID Program], https://gwdac.phys.gwu.edu/analysis/pin_analysis.html/.

[76] R. Koch and E. Pietarinen, Low-energy πN partial wave analysis, Nucl. Phys. A **336**, 331 (1980).

[77] https://pwa.hiskp.uni-bonn.de.

[78] V. I. Mokeev, V. D. Burkert, T. S. H. Lee, L. Elouadrhiri, G. V. Fedotov, and B. S. Ishkhanov, Model analysis of the $ep \to e'p\pi^+\pi^-$ electroproduction reaction on the proton, Phys. Rev. C **80**, 045212 (2009).

[79] V. I. Mokeev *et al.* (CLAS Collaboration), Experimental study of the $P_{11}(1440)$ and $D_{13}(1520)$ resonances from the CLAS data on $ep \to e'\pi^+\pi^- p'$, Phys. Rev. C **86**, 035203 (2012).

[80] N. M. Kroll and M. A. Ruderman, A theorem on photomeson production near threshold and the suppression of pairs in pseudoscalar meson theory, Phys. Rev. **93**, 233 (1954).

[81] M. Guidal, J. M. Laget and M. Vanderhaeghen, Pion and kaon photoproduction at high-energies: Forward and intermediate angles, Nucl. Phys. A **627**, 645 (1997).

[82] P. Söding, On the apparent shift of the rho meson mass in photoproduction, Phys. Lett. **19**, 702 (1966).

[83] M. H. Ross and L. Stodolsky, Photon dissociation model for vector meson photoproduction, Phys. Rev. **149**, 1172 (1966).

[84] J. Breitweg *et al.* (ZEUS Collaboration), Elastic and proton dissociative ρ^0 photoproduction at HERA, Eur. Phys. J. C **2**, 247 (1998).

[85] K. Schilling, P. Seyboth and G. E. Wolf, On the Analysis of Vector Meson Production by Polarized Photons, Nucl. Phys. B **15**, 397 (1970) [**18**, 332(E) (1970)].

[86] H. S. Song, Spin 3/2 polarization density matrix in the electroproduction of $\Delta(1236)$, Phys. Rev. D **8**, 820 (1973).

[87] V. Burkert *et al.*, Note on the definitions of branching ratios of overlapping resonances, Phys. Lett. B **844**, 138070 (2023).

[88] R. L. Workman *et al.* (Particle Data Group), Review of particle physics, Prog. Theor. Exp. Phys. **2022**, 083C01 (2022).

[89] M. Shrestha and D. M. Manley, Multichannel parametrization of πN scattering amplitudes and extraction of resonance parameters, Phys. Rev. C **86**, 055203 (2012).

[90] T. P. Vrana, S. A. Dytman and T. S. H. Lee, Baryon resonance extraction from πN data using a unitary multichannel model, Phys. Rep. **328**, 181 (2000).

[91] B. C. Hunt and D. M. Manley, Updated determination of N^* resonance parameters using a unitary, multichannel formalism, Phys. Rev. C **99**, 055205 (2019).